This is the peer-reviewed, final accepted version for American Mineralogist, published by the Mineralogical Society of America.
The published version is subject to change. Cite as Authors (Year) Title. American Mineralogist, in press.
DOI: https://doi.org/10.2138/am-2022-8552. http://www.minsocam.org/

Revision 4 (Clean)

Lead and noble gas isotopic constraints on the origin of Te-bearing adularia-sericite epithermal Au-Ag deposits in a calc-alkaline magmatic arc, NE China

Shen Gao[1, 2*] (***Corresponding Author***), Albert H. Hofstra[3], Kezhang Qin[2, 4*] (***Corresponding Author***), Xinyu Zou[2], Michael J. Pribil[3], Andrew G. Hunt[3], Andrew H. Manning[3], Heather A. Lowers[3], Hong Xu[1]

[1] *School of Earth Sciences and Resources, China University of Geosciences (Beijing), Beijing 100083, China*

[2] *Key Laboratory of Mineral Resources, Institute of Geology and Geophysics, Chinese Academy of Sciences, Beijing 100029, China*

[3] *U.S. Geological Survey, P.O. Box 25046, Denver, CO 80225, USA*

[4] *University of Chinese Academy of Sciences, Beijing 100049, China*

Submitted to: **American Mineralogist**

Submission date: **04/14/2022**

Revision 1 date: **04/20/2023**

Revision 2 date: **07/21/2023**

Revision 3 date: **11/17/2023**

Revision 4 date: 12/05/2023

Always consult and cite the final, published document. See http:/www.minsocam.org or GeoscienceWorld

This is the peer-reviewed, final accepted version for American Mineralogist, published by the Mineralogical Society of America.
The published version is subject to change. Cite as Authors (Year) Title. American Mineralogist, in press.
DOI: https://doi.org/10.2138/am-2022-8552. http://www.minsocam.org/

Abstract

Tellurium (Te)-bearing adularia-sericite epithermal Au-Ag deposits are widely distributed in calc-alkaline magmatic arcs and are an important current and future source of precious and critical metals. The source of ore-forming fluids in these deposits remains unclear due to the lack of in-situ isotopic evidence on Au-, Ag-, and Te-bearing minerals. To advance the understanding of the source and evolution of Te and precious metals, herein, we combine in situ Pb isotope analysis with He, Ne, and Ar isotope and microthermometric analysis of fluid inclusions in ore and gangue minerals from two Te-rich and two Te-poor epithermal Au-Ag deposits that occur in an Early Cretaceous magmatic arc in the North Heilongjiang Belt, northeastern China. Ore minerals (hessite, petzite, calaverite, altaite, pyrite, chalcopyrite, and galena) from Te-rich Au-Ag deposits, including Sandaowanzi and Yongxin, have the least radiogenic Pb isotope compositions ($^{206}Pb/^{204}Pb$ from 18.1 to 18.3) and the lowest μ1 values (the $^{238}U/^{204}Pb$ ratio of the lead source down to 9.14) of the deposits studied. For these Te-rich deposits, noble gas isotope data show that fluid inclusions in ore minerals contain a large proportion of mantle He (up to 25%) whereas barren early-stage minerals do not (<1%). The Pb, noble gas isotope, and fluid inclusion microthermometric results suggest that Te-rich ore-forming fluids were likely discharged from mafic magmas into convecting meteoric flow systems at shallow levels (<2 km). In contrast to the Te-rich deposits, ore minerals from the Te-poor Dong'an Au-Ag deposit have radiogenic Pb isotope compositions

Always consult and cite the final, published document. See http:/www.minsocam.org or GeoscienceWorld

This is the peer-reviewed, final accepted version for American Mineralogist, published by the Mineralogical Society of America.
The published version is subject to change. Cite as Authors (Year) Title. American Mineralogist, in press.
DOI: https://doi.org/10.2138/am-2022-8552. http://www.minsocam.org/

42 ($^{206}Pb/^{204}Pb$ from 18.8 to 18.9) and the highest μ1 values (up to 10.54). Fluid inclusions
43 in ore minerals contain a small proportion of mantle He (1% to 5%). The results suggest
44 that metals and ore-forming fluids in these deposits were discharged from either more
45 crustally contaminated intermediate-felsic magmas or leached from upper crustal rocks
46 by convecting meteoric flow systems. Although the Te-poor Tuanjiegou Au-Ag deposit
47 has a non-radiogenic Pb isotope composition consistent with a mafic magma source, Te is
48 much less abundant (electrum [>95%] is the major gold- and silver-bearing mineral) than
49 Au. The main exploration implication of these results is that unexplored volcano-plutonic
50 centers in the northeast Xing'an Block with less radiogenic Pb isotope compositions
51 ($^{206}Pb/^{204}Pb < 18.3$) and containing fluids having a high proportion of mantle He are more
52 likely to generate Te-rich epithermal Au-Ag deposits than other volcano-plutonic centers
53 in NE China.
54
55 **Key words:** In situ Pb isotope, Noble gas, Te, Epithermal, Au-Ag deposit, NE China.
56
57 **1. Introduction**
58
59 Tellurium (Te)-bearing adularia-sericite epithermal Au-Ag deposits are often
60 associated with calc-alkalic volcano-plutonic centers, such as those in the Golden
61 Quadrilateral, Romania, numerous Cretaceous-Quaternary deposits in Japan, and Early
62 Cretaceous deposits in northeastern China (Shikazono et al. 1990; Ciobanu et al. 2006;

Always consult and cite the final, published document. See http:/www.minsocam.org or GeoscienceWorld

Cook et al. 2009; Sun et al. 2013; Goldfarb et al. 2016, 2017; Gao et al. 2017a, 2018a, 2021, 2022; White et al. 2019; Keith et al. 2020), although many deposits are associated with alkalic volcano-plutonic centers (e.g., Cripple Creek, Colorado, USA; Kelley et al. 1998, 2016). These Te-bearing deposits are economically important and are a potential source of Te, which is a critical commodity for modern technology, if current metallurgical and economic impediments are resolved (Spry et al. 2004; Ciobanu et al. 2006; Cook et al. 2009; Kelley and Spry 2016; Goldfarb et al. 2016, 2017; Jenkin et al. 2019).

The source of Te in these deposits is generally thought to be derived from igneous intrusions in continental magmatic belts that metasomatized subcontinental lithospheric mantle (SCLM) during subduction (Jensen and Barton 2000; Saunders and Brueseke 2012; Kelley and Spry 2016; Holwell et al. 2019). However, the abundance of Te-bearing minerals varies among adularia-sericite epithermal Au-Ag deposits within the same calc-alkaline magmatic arc, e.g., Te-rich Sandaowanzi and Te-poor Dong'an deposits in NE China (Zhang et al. 2010; Yu et al. 2012; Han 2013; Liu et al. 2013; Zhai et al. 2015, 2018; Gao et al. 2017a, 2021; Zhao et al. 2019a, b and reference therein). This observation suggests that the source of and/or enrichment process for Te vary in each Au-Ag deposit in the arc. Previous work on the S, Pb, H, O, He, and Ar isotopic composition of Te-bearing epithermal Au-Ag deposits in NE China suggests that they formed from a mixture of magmatic fluids and meteoric water (e.g., Zhai et al. 2015, 2018; Li 2018; Zhao et al. 2019b). Similar evidence has been obtained from classic

Always consult and cite the final, published document. See http:/www.minsocam.org or GeoscienceWorld

This is the peer-reviewed, final accepted version for American Mineralogist, published by the Mineralogical Society of America.
The published version is subject to change. Cite as Authors (Year) Title. American Mineralogist, in press.
DOI: https://doi.org/10.2138/am-2022-8552. http://www.minsocam.org/

84 adularia-sericite epithermal Au-Ag deposits in other parts of the world (e.g., Baguio
85 district, Philippines; Mule Canyon, Nevada, USA; Cooke and Simmons 2000; John et al.
86 2003a, b, 2018). However, these studies have not identified the source and evolution of
87 Te-bearing fluids due to the lack of in situ analysis of ore minerals, e.g., altaite (PbTe),
88 petzite (Ag_3AuTe_2), and hessite (Ag_2Te). Thus, the role of magmatic fluids in the
89 formation of Te-rich and Te-poor adularia-sericite epithermal Au-Ag deposits within the
90 same arc remains unknown.

91 To advance understanding of the source of Te, precious metals, volatiles, and fluid
92 evolution in adularia-sericite epithermal Au-Ag deposits within a calc-alkaline magmatic
93 arc, we studied the Te-rich Sandaowanzi and Yongxin deposits in the Xing'an Block, and
94 the Te-poor Dong'an deposit in the Songliao Block and the Tuanjiegou deposit in the
95 Jiamusi Massif. We conducted in situ femtosecond laser ablation Pb isotope analysis on
96 telluride minerals, coexisting sulfide minerals, and hydrothermal gangue minerals in the
97 veins together with high-resolution isotope analysis of He, Ne, and Ar extracted from
98 fluid inclusions and fluid inclusion microthermometry. The results are used to determine
99 the proportions of mantle and crustal material in Te-rich and Te-poor Au-Ag deposits. For
100 example, He sources include 10–40 R/R_A (where R/R_A is the $^3He/^4He$ ratio of air,
101 1.384×10^{-6}) for the primitive mantle; 7–9 R/R_A for shallow depleted mantle; ~1 R/R_A for
102 air-saturated meteoric water; and ~0.02 R/R_A for crustal fluids (Graham 2002; Hilton et
103 al. 2002). In addition, this is also the first in situ study of Pb isotopes in tellurides
104 (including altaite, petzite, and hessite) from an epithermal system that has been conducted

Always consult and cite the final, published document. See http:/www.minsocam.org or GeoscienceWorld

using a femtosecond laser ablation MC-ICP-MS. The isotopic results obtained on low Pb content minerals are useful and important for tracing the source of metals in hydrothermal deposits.

2. Geological framework and deposit setting

The study area is located in the eastern part of the Paleozoic Central Asian Orogenic Belt (CAOB) (Sengör et al. 1993; Jahn et al. 2000; Jahn 2004; Li 2006). The CAOB consists of the Erguna and Xing'an Blocks in the northwest, the Songliao Block in the central part, and the Jiamusi Massif in the east, which are separated by the De'erbugan, Nenjiang-Heihe, and Jiayin-Mudanjiang structures, respectively (Fig. 1a) (Wu et al. 2007). The adularia-sericite epithermal Au-Ag deposits studied are located in the Xing'an and Songliao Block, and the Jiamusi Massif (Fig. 1a; e.g., Sun et al. 2013; Wang et al. 2016; Song et al. 2019; Gao et al. 2021; Wang et al. 2021).

The Xing'an Block is dominated by Mesozoic igneous rocks (Ge et al. 2005; Sui et al. 2007; Zhang et al. 2008) and Neoproterozoic-Lower Cambrian metamorphic rocks, e.g., Luomahu Group (Qu 2008; Fig. 1a). Although sedimentation occurred during the Neoproterozoic and Paleozoic (Miao et al. 2004, 2007, 2015), metamorphism and deformation occurred in these blocks during the Jurassic (ca. 170–160 Ma; Miao et al. 2015; Fig. 1b) producing a lithologic assemblage that is dominated by mica and two-mica-plagioclase gneisses, marbles, and the garnet-sillimanite-staurolite-bearing

Always consult and cite the final, published document. See http:/www.minsocam.org or GeoscienceWorld

two-mica quartz schist (e.g., Miao et al. 2015). The Songliao Block is largely covered by Lower Cretaceous volcanic rocks (Wang et al. 2002; Zhang et al. 2007; Shu et al. 2007; Ding et al. 2007) with local exposures of underlying granitoids and Precambrian rocks (Wu et al. 2000; Wang et al. 2006; Pei et al. 2007; Gao et al. 2007; Xu et al. 2008; Zhang et al. 2008) (Fig. 1b). The Jiamusi Massif consists of the Mashan Complex, the Heilongjiang Complex, Cambrian and Permian granitoids and Lower Cretaceous volcanic rocks. The Mashan Complex contains schists, gneisses, and marbles metamorphosed to the granulite facies (metamorphic age: ca. 500 Ma) (Wilde et al. 1997, 2000). The Heilongjiang Complex consists of mafic-ultramafic rocks, various quartz-feldspathic schists, and radiolarian-bearing quartzites (formerly cherts) (Zhou et al. 2009). Two types of granitoids, including deformed and metamorphosed Cambrian granitoids (ca. 520 Ma) (Wilde et al. 2003) and weakly deformed to undeformed Permian granites (ca. 260 Ma), are documented in the Jiamusi massif (Wilde et al. 1997; Wu et al. 2000).

Regional structures mainly consist of NE- and NW-trending faults. The Nenjiang-Heihe fault and Jiayin-Mudanjiang fault control the distribution of gold deposits in the area (Fig. 1a). Mesoproterozoic intrusions include biotite-plagioclase-gneisses. Carboniferous intrusions consist of mylonitized diorite, tonalite, and monzogranite, Early Permian intrusions are alkali-feldspar granites, and Triassic-Jurassic intrusions consist of monzogranite and granodiorite (ca. 150–190 Ma; Sui et al. 2007; Zhao et al. 2015; Gao et al. 2018b). Early Cretaceous granites were emplaced in an extensional setting related to subduction of the Paleo-Pacific Plate (e.g.,

Always consult and cite the final, published document. See http:/www.minsocam.org or GeoscienceWorld

This is the peer-reviewed, final accepted version for American Mineralogist, published by the Mineralogical Society of America.
The published version is subject to change. Cite as Authors (Year) Title. American Mineralogist, in press.
DOI: https://doi.org/10.2138/am-2022-8552. http://www.minsocam.org/

147 Wu et al. 2007).

148 The Pb isotope framework of the northern Heilongjiang province and the geology of
149 the Sandaowanzi, Yongxin, Dong'an, and Tuanjiegou deposits are described in Appendix
150 A (Fig. A1–A2; Fig. 2). The main features of each deposit are summarized in Table 1 and
151 briefly described below. In these deposits, igneous rocks and hydrothermal minerals are
152 similar in age. The Sandaowanzi deposit has an older age (~120 Ma; e.g., Liu et al., 2011,
153 Gao et al., 2017a) than the Yongxin deposit (~114 Ma; e.g., Zhao et al. 2019a, b). Both
154 the Dong'an and the Tuanjiegou deposits have the youngest ages (~108 Ma; e.g., Zhang
155 et al. 2010; Wang et al. 2012).

156

157 **3. Sampling and methods**

158

159 **3.1. Sample collection and description**

160

161 Fresh hand samples from Sandaowanzi, Yongxin, Dong'an, and Tuanjiegou were
162 collected from underground mines, open pits, and drill holes (Table 2; Fig. 3). The
163 samples were obtained from veins or host rock close to the veins, and they are all fresh
164 without any weathering rims. Ore mineral-bearing thick sections (~200 μm) were used to
165 conduct in situ Pb isotope analyses. Sixteen minerals were analyzed (samples shown in
166 Figs. 3–4, Appendix Fig. A3), including tellurides (stützite: Ag_7Te_4, hessite: Ag_2Te,
167 sylvanite: $AuAgTe_4$, petzite: Ag_3AuTe_2, calaverite: $AuTe_2$, and altaite: PbTe), sulfides

Always consult and cite the final, published document. See http:/www.minsocam.org or GeoscienceWorld

(pyrite: FeS_2, chalcopyrite: $CuFeS_2$, sphalerite: ZnS, argentite: Ag_2S, and galena: PbS), silicates (adularia: $KAlSi_3O_8$, plagioclase: $(Na, Ca)[(Si, Al)AlSi_2]O_8$, and sericite: $KAl_2(AlSi_3O_{10})(OH)_2$), carbonate (calcite: $CaCO_3$), and sulfosalt (freibergite: $Ag_6[Cu_4Fe_2]Sb_4S_{12}$). Analyzed minerals such as stützite, calaverite, freibergite, chalcopyrite, and sericite had signals that were too low for ^{204}Pb and/or too high signals of ^{202}Hg, in which case the ^{204}Pb-related data were not used for discussion. Instead, the other three Pb isotopes (^{206}Pb, ^{207}Pb, and ^{208}Pb) are presented (Table 3).

Samples analyzed for noble gas isotopes are listed in Table 2 and are composed of gangue mineral separates and sulfide separates. Mineralized pyrites containing electrum/telluride inclusions were collected from quartz-pyrite veins in the Yongxin and Tuanjiegou deposits. Unmineralized pyrites in the host volcanic rocks that formed by alteration were collected from Sandaowanzi. Ore-bearing quartz veins including sulfides, electrum, and tellurides were collected from each deposit. Late-stage veins containing calcite and fluorite are barren and usually cut main stage veins. In general, a single vein stage was analyzed to avoid mixing multiple veins in the same sample.

Hand samples were first crushed to a large grain size (~2 mm) and sieved. These grains were ultrasonically cleaned in distilled water. After drying at room temperature, mineral separates of quartz, adularia, calcite, fluorite, and pyrite were handpicked under a binocular microscope. The dried separates were then put in glass bottles with a cover. Prior to analysis, each separate was cleaned in distilled water and methanol. The images on Figure 5 are representative of the textures, mineral assemblages, and fluid inclusions

Always consult and cite the final, published document. See http:/www.minsocam.org or GeoscienceWorld

(also see Fig. 6) present in the samples. Most samples are dominated by primary inclusions in crystal cores and growth zones, with minor secondary inclusions in fractures.

3.2. Femtosecond Laser Ablation MC-ICP-MS

In situ Pb isotope ratio analyses were conducted at the U.S. Geological Survey High Resolution Laboratory in Denver, Colorado using femtosecond (*fs*) laser ablation multicollector inductively coupled plasma mass spectrometry (*fs* LA-MC-ICP-MS). A Teledyne Photon Machines Excite Pharos *fs* laser ablation system (Teledyne, USA) was coupled to a Nu Plasma 2 MC-ICP-MS (Nu Instruments, UK). Ablated sample aerosols were carried from the laser ablation cell to the MC-ICP-MS using He carrier gas. Laser ablation parameters varied dependent on Pb concentration and mineral grain size. Laser beam energy applied to the sample surface is dependent on beam diameter and ranged from 4.1 J/cm^2 for 75 µm spot size to 7.5 J/cm^2 for 30 µm spot size with laser power ranging from 8 to 90%. Beam size for line and spot analyses ranged from 5 to 75µm (beam aperture variable from 1 to 75 µm at 1 µm resolution) and the repetition rate varied from 6 to 30 Hz. Larger beam sizes (e.g., 75 µm) were used for lead-poor Au-Ag tellurides whereas smaller sizes (10–15 µm) were used for lead-rich galena and altaite. A wavelength of 257 nm was used for all analyses. A line scan rate of 5 µm per second was used for all line analyses.

Always consult and cite the final, published document. See http:/www.minsocam.org or GeoscienceWorld

This is the peer-reviewed, final accepted version for American Mineralogist, published by the Mineralogical Society of America.
The published version is subject to change. Cite as Authors (Year) Title. American Mineralogist, in press.
DOI: https://doi.org/10.2138/am-2022-8552. http://www.minsocam.org/

The MC-ICP-MS system simultaneously collected ^{202}Hg, ^{203}Tl, ^{204}Pb, ^{205}Tl, ^{206}Pb, ^{207}Pb, and ^{208}Pb signals on Faraday cups during each analysis. Correction for ^{204}Hg was automatically implemented via data acquisition software for samples with measurable ^{202}Hg signal. Mass bias was corrected using National Institute of Standards and Technology (NIST) isotopic standard reference material (SRM) for thallium (SRM 997). A prepared solution of SRM 997 was introduced to the laser ablation sample stream prior to the MC-ICP-MS using an Aridus II (Cetac, USA) desolvating nebulizer. Mass bias was corrected using the exponential law with ^{205}Tl/^{203}Tl for SRM 997 of 2.3871 and isotope pair correction (Woodhead et al. 2002).

A mixed solution of NIST SRM 981 (20 ug/L) and NIST SRM 997 (2 ug/L) was analyzed prior to the laser ablation session (daily and between long breaks) to tune the MC-ICP-MS and verify the accuracy and precision of the instrument in solution mode. The femtosecond laser ablation system was coupled to the MC-ICP-MS once the Pb isotope ratio measurements for SRM 981 in solution were within error of reference values previously reported for NIST SRM 981 (Galer and Abouchami 1998). Two USGS glasses, PB-ISO-1G and GSE-2G, were used to determine standard deviation and reproducibility for femtosecond laser ablation sample introduction. The USGS PB-ISO-1G in-house glass is a basalt material spiked with NIST SRM 981 at 250 ug/g and prepared in a similar manner as other USGS glasses. The Pb isotope ratios were validated by solution and laser introduction and results are within error of previously reported values for NIST SRM 981 by Galer and Abouchami (1998); ^{208}Pb/^{204}Pb =

Always consult and cite the final, published document. See http:/www.minsocam.org or GeoscienceWorld

This is the peer-reviewed, final accepted version for American Mineralogist, published by the Mineralogical Society of America.
The published version is subject to change. Cite as Authors (Year) Title. American Mineralogist, in press.
DOI: https://doi.org/10.2138/am-2022-8552. http://www.minsocam.org/

231 36.722 ± 0.004, $^{207}Pb/^{204}Pb$ = 15.496 ± 0.002, and $^{206}Pb/^{204}Pb$ = 16.941 ± 0.002 (Table 3).
232 The PB-ISO-1G was analyzed two to three times prior to the start of each session and
233 periodically between samples and resulted in an average $^{208}Pb/^{204}Pb$ = 36.718 ± 0.013,
234 $^{207}Pb/^{204}Pb$ = 15.489 ± 0.006, and $^{206}Pb/^{204}Pb$ = 16.946 ± 0.008 (n = 11, 2s; Table 3). The
235 USGS GSE-2G glass resulted in an average $^{208}Pb/^{204}Pb$ = 39.143 ± 0.016, $^{207}Pb/^{204}Pb$ =
236 15.771 ± 0.007, and $^{206}Pb/^{20t4}Pb$ = 19.907 ± 0.009 (n=15, 2s; Table 3).
237
238 **3.3. High-resolution sector mass spectrometry**
239
240 Noble gases (He, Ne, and Ar) in fluid inclusions were extracted from 20 samples by
241 thermal decrepitation and analyzed using a mass spectrometer. The analytical method and
242 interpretation schemes are those described by Landis and Hofstra (2012), Hofstra et al.
243 (2016) and Manning and Hofstra (2017). Each 0.5- to 1.5-g mineral separate was
244 drop-loaded into a preheated, evacuated vacuum furnace, heated to 350 °C, and held at
245 temperature for 10 to 30 min to collect volatiles for analysis. Reactive gases were
246 chemically removed from the gas mixture and the remaining noble gases were
247 cryogenically separated (liquid nitrogen trap at 77 °K and helium refrigerant trap at 9 °K),
248 prior to determinations of noble gas abundance and isotopic compositions with a static
249 high-resolution sector mass spectrometer (Helix-SFT). Gas concentrations were
250 determined by calibration to a known air standard with an average sample-to-standard
251 ratio of two (Manning and Hofstra, 2017). Details are provided in Hunt (2015) and Hunt

Always consult and cite the final, published document. See http:/www.minsocam.org or GeoscienceWorld

This is the peer-reviewed, final accepted version for American Mineralogist, published by the Mineralogical Society of America.
The published version is subject to change. Cite as Authors (Year) Title. American Mineralogist, in press.
DOI: https://doi.org/10.2138/am-2022-8552. http://www.minsocam.org/

et al. (2023).

3.4. Microthermometry

In representative samples, fluid inclusion assemblages were observed in crystalline quartz, calcite, and fluorite. Fluid inclusions > 5 μm in size were analyzed and correlated with the noble gas analysis. Fluid inclusion petrography and microthermometry were conducted at the Key Laboratory of Mineral Resources, Institute of Geology and Geophysics, Chinese Academy of Sciences. A Linkman 600 heating/freezing stage on an Olympus BX60 microscope was used to measure the ice melting temperature and homogenization temperature of fluid inclusions in each assemblage. A pure H_2O standard with an ice melting temperature (T_m) of 0 °C and a critical homogenization temperature (T_h) of 373.6 °C was used to calibrate the stage with the data reproducible to ± 0.2 °C for ice melting temperatures and ± 2.0 °C for homogenization temperatures.

4. Results

4.1. Pb isotope compositions

Due to complex intergrowths of fine-grained tellurides, sulfides, and gangue minerals, Pb isotope analyses were conducted using in situ methods (Fig. 4; Appendix A

Always consult and cite the final, published document. See http:/www.minsocam.org or GeoscienceWorld

This is the peer-reviewed, final accepted version for American Mineralogist, published by the Mineralogical Society of America.
The published version is subject to change. Cite as Authors (Year) Title. American Mineralogist, in press.
DOI: https://doi.org/10.2138/am-2022-8552. http://www.minsocam.org/

Fig. A3). Eleven minerals (altaite, hessite, petzite, sylvanite, galena, sphalerite, pyrite, argentite, adularia, calcite, and plagioclase) were analyzed and the data are reported in Table 3. In Table 3, "nd" (not determined) was due to insufficient ^{204}Pb signal, as we did not report data where the ^{204}Pb signal was below 50mV. The total signal for our reported Pb isotope ratios was greater than 3 volts and most samples were 10 volts and higher.

At Sandaowanzi, main stage minerals have a narrow range of Pb isotope compositions. The ranges of ^{206}Pb/^{204}Pb, ^{207}Pb/^{204}Pb, and ^{208}Pb/^{204}Pb values are 18.263 to 18.285, 15.525 to 15.542, and 38.105 to 38.173, respectively. The ^{207}Pb/^{206}Pb values range from 0.8486 to 0.8592 (average SE 0.0001), whereas the ^{208}Pb/^{206}Pb values range from 2.0824 to 2.1082 (average SE 0.0003). The radiogenic Pb isotope composition of early-stage pyrite in host rocks ranges from 0.8492 to 0.8538 in ^{207}Pb/^{206}Pb values (average SE 0.0001) and from 2.0844 to 2.0936 in ^{208}Pb/^{206}Pb values (average SE 0.0003).

At Yongxin, main-stage altaite and galena have similar Pb isotope compositions. The ranges of ^{206}Pb/^{204}Pb, ^{207}Pb/^{204}Pb, and ^{208}Pb/^{204}Pb values are 18.127 to 18.139, 15.509 to 15.526, and 37.949 to 37.976, respectively. The ^{207}Pb/^{206}Pb values range from 0.8557 to 0.8563 (average SE 0.0001), and the ^{208}Pb/^{206}Pb values range from 2.0935 to 2.0946 (average SE 0.0003). The radiogenic Pb isotope composition of main stage pyrite ranges from 0.8535 to 0.8560 in ^{207}Pb/^{206}Pb values (average SE 0.0001) and from 2.0902 to 2.0936 in ^{208}Pb/^{206}Pb values (average SE 0.0003).

At Dong'an, the Pb isotope compositions of tellurides and sulfides also have a

Always consult and cite the final, published document. See http:/www.minsocam.org or GeoscienceWorld

This is the peer-reviewed, final accepted version for American Mineralogist, published by the Mineralogical Society of America.
The published version is subject to change. Cite as Authors (Year) Title. American Mineralogist, in press.
DOI: https://doi.org/10.2138/am-2022-8552. http://www.minsocam.org/

294 relatively narrow range. The ranges of $^{206}Pb/^{204}Pb$, $^{207}Pb/^{204}Pb$, and $^{208}Pb/^{204}Pb$ values are
295 18.822 to 18.909, 15.574 to 15.610, and 38.423 to 38.573, respectively. The composition
296 of $^{207}Pb/^{206}Pb$ ranges from 0.8251 to 0.8284 (average SE 0.0001) and $^{208}Pb/^{206}Pb$ ranges
297 from 2.0384 to 2.0440 (average SE 0.0003).

298 At Tuanjiegou, main stage galena and pyrite have $^{206}Pb/^{204}Pb$, $^{207}Pb/^{204}Pb$, and
299 $^{208}Pb/^{204}Pb$ values that range from 18.272 to 18.317, 15.521 to 15.544, and 38.161 to
300 38.221, respectively. The $^{207}Pb/^{206}Pb$ values range from 0.8488 to 0.8501 (average SE
301 0.0001) and the $^{208}Pb/^{206}Pb$ values range from 2.0866 to 2.0903 (average SE 0.0003).

302

303 **4.2. Noble gas isotope compositions**

304

305 Twenty mineral separates composed of quartz, adularia, fluorite, calcite, or pyrite
306 were analyzed for He, Ne, and Ar, including four from Sandaowanzi, five from Yongxin,
307 seven from Dong'an, and four from Tuanjiegou (Fig. 5; Table 4).

308 At Sandaowanzi, main stage quartz has helium R/R_A values from 0.064 to 0.340 with
309 an average uncertainty of 0.020. ^{4}He concentrations range from 0.010 to 0.151 μcc/g with
310 an average uncertainty of 0.011. ^{20}Ne concentrations range from 0.003 to 0.042 μcc/g
311 with an average uncertainty of 0.001, $^{20}Ne/^{22}Ne$ and $^{21}Ne/^{22}Ne$ have narrow ranges of
312 9.779 to 9.965 and 0.0275 to 0.0293, respectively. ^{40}Ar concentrations range from 37.555
313 to 120.092 μcc/g with an average uncertainty of 1.816, and the samples have a narrow
314 range of $^{40}Ar/^{36}Ar$ ratios from 287.6 to 289.6 and $^{38}Ar/^{36}Ar$ ratios from 0.1880 to 0.1882.

Always consult and cite the final, published document. See http:/www.minsocam.org or GeoscienceWorld

315 At Yongxin, main stage pyrite and quartz as well as later stage calcite have the
316 highest helium R/R_A values from 0.055 to 1.698 with an average uncertainty of 0.050.
317 ^{4}He concentrations range from 0.147 to 3.648 μcc/g with an average uncertainty of 0.056.
318 The Ne isotope values are higher than Sandaowanzi. ^{20}Ne concentrations range from
319 0.014 to 0.172 μcc/g with an average uncertainty of 0.002, $^{20}Ne/^{22}Ne$ and $^{21}Ne/^{22}Ne$ have
320 narrow ranges of 9.818 to 10.120 and 0.0287 to 0.0293, respectively. ^{40}Ar concentrations
321 range from 50.210 to 478.419 μcc/g with an average uncertainty of 3.985, and the
322 samples have a narrow range of $^{40}Ar/^{36}Ar$ ratios from 268.3 to 303.0 and $^{38}Ar/^{36}Ar$ ratios
323 from 0.1878 to 0.1939.

324 At Dong'an, quartz, pyrite, adularia, and fluorite have helium R/R_A values from
325 0.028 to 0.926 with an average uncertainty of 0.038. ^{4}He concentrations range from 0.009
326 to 2.261 μcc/g with an average uncertainty of 0.033. Dong'an has the lowest ^{20}Ne
327 concentrations with a range from 0.002 to 0.011 μcc/g with an average uncertainty of
328 0.0001. $^{20}Ne/^{22}Ne$ and $^{21}Ne/^{22}Ne$ have narrow ranges of 9.891 to 10.168 and 0.0258 to
329 0.0301, respectively. ^{40}Ar concentrations range from 11.216 to 26.037 μcc/g with an
330 average uncertainty of 0.429, and the samples have a narrow range of $^{40}Ar/^{36}Ar$ ratios
331 from 275.3 to 291.6 and $^{38}Ar/^{36}Ar$ ratios from 0.1773 to 0.1913.

332 At Tuanjiegou, main stage pyrite and quartz as well as later stage calcite have helium
333 R/R_A values from 0.135 to 0.528 with an average uncertainty of 0.032. ^{4}He
334 concentrations range from 0.006 to 0.525 μcc/g with an average uncertainty of 0.013, and
335 ^{20}Ne concentrations range from 0.002 to 0.172 μcc/g with an average uncertainty of 0.001,

Always consult and cite the final, published document. See http:/www.minsocam.org or GeoscienceWorld

This is the peer-reviewed, final accepted version for American Mineralogist, published by the Mineralogical Society of America.
The published version is subject to change. Cite as Authors (Year) Title. American Mineralogist, in press.
DOI: https://doi.org/10.2138/am-2022-8552. http://www.minsocam.org/

$^{20}Ne/^{22}Ne$ and $^{21}Ne/^{22}Ne$ have narrow ranges of 9.707 to 10.046 and 0.0290 to 0.0294, respectively. Tuanjiegou has the highest ^{40}Ar concentrations from 5.283 to 906.175 μcc/g with an average uncertainty of 5.637. The samples have a range of $^{40}Ar/^{36}Ar$ ratios from 248.8 to 291.9 and $^{38}Ar/^{36}Ar$ ratios from 0.1782 to 0.1905.

4.3. Fluid inclusion microthermometry

Thirty-five doubly polished sections composed of quartz, fluorite, and calcite were used for fluid inclusion petrography and microthermometric analyes of ice melting and homogenization temperatures, including three from Sandaowanzi, seventeen from Yongxin, nine from Dong'an, and six from Tuanjiegou (Table 5; Appendix B Table B1). Additional data on fluid inclusions in quartz from Sandaowanzi (thirty-four samples) and Dong'an (two samples) were compiled from Gao (2017) and Gao et al. (2021), and fluid inclusions in fluorite (N=74) from Dong'an were compiled from Zhi (2015). Ice melting temperatures were used to calculate salinity (Hall et al. 1988). Fluid inclusion data from early-, main-, and late-stage minerals were used in this study. Early stage is I, the main stage includes II-IV, and the late stage is V. Although Yongxin quartz contains CO_2-bearing fluid inclusions (Fig. 6f, g), they were too small (<5 μm) for microthermometry. Others are L-V type in the H_2O-NaCl system (Fig. 6).

At Sandaowanzi (Te-rich), fluid inclusions in the early stage have a large range of homogenization temperatures from 226 to 361 °C and salinities that range from 0.2 to

Always consult and cite the final, published document. See http:/www.minsocam.org or GeoscienceWorld

This is the peer-reviewed, final accepted version for American Mineralogist, published by the Mineralogical Society of America.
The published version is subject to change. Cite as Authors (Year) Title. American Mineralogist, in press.
DOI: https://doi.org/10.2138/am-2022-8552. http://www.minsocam.org/

12.9 eq. wt. % NaCl, in the main stage homogenization temperatures range from 186 to 309 °C and salinities range from 0.2 to 9.6 eq. wt. % NaCl, and in the late stage homogenization temperatures range from 110 to 211 °C and salinities range from 0.2 to 8.5 eq. wt. % NaCl (Table 5; Appendix B Table B1). At Yongxin (Te-rich), fluid inclusions in the early stage have high homogenization temperatures that range from 328 to 341 °C and salinities that range from 6.0 to 8.3 eq. wt. % NaCl, in the main stage homogenization temperatures range from 178 to 297 °C and salinities range from 3.0 to 9.2 eq. wt. % NaCl. Late stage homogenization temperatures range from 117 to 207 °C and salinities have high values up to 11.2 eq. wt. % NaCl (Table 5; Appendix B Table B1). At Dong'an (Te-poor), fluid inclusions in the early stage have lower homogenization temperatures from 260 to 290 °C and salinities that range from 0.2 to 4.9 eq. wt. % NaCl, in the main stage homogenization temperatures range from 223 to 256 °C and salinities range from 0.2 to 3.0 eq. wt. % NaCl, and in the late stage homogenization temperatures range from 120 to 190 °C and salinities range from 0.4 to 3.2 eq. wt. % NaCl (Table 5; Appendix B Table B1). All stages at Dong'an have lower salinities than the other four deposits. At Tuanjiegou (Te-poor), fluid inclusions in the early stage have homogenization temperatures that range from 261 to 280 °C and salinities that range from 1.8 to 2.2 eq. wt. % NaCl, in the main stage homogenization temperatures range from 208 to 254 °C and salinities range from 2.2 to 7.9 eq. wt. % NaCl, and in the late stage homogenization temperatures range from 162 to 171 °C and salinities range from 2.2 to 3.4 eq. wt. % NaCl (Table 5; Appendix B Table B1).

Always consult and cite the final, published document. See http:/www.minsocam.org or GeoscienceWorld

This is the peer-reviewed, final accepted version for American Mineralogist, published by the Mineralogical Society of America.
The published version is subject to change. Cite as Authors (Year) Title. American Mineralogist, in press.
DOI: https://doi.org/10.2138/am-2022-8552. http://www.minsocam.org/

5. Discussion

5.1. Lead isotopes

5.1.1. Lead sources

Lead isotope compositions are a useful tool to constrain the source and evolution of ore-forming fluids in hydrothermal deposits (e.g., Gulson 1986; Foley and Ayuso 1994; Richards et al. 1991; Richards and Noble 1998; Bouse et al. 1999; Tosdal et al. 1999, 2003; Hofstra et al. 2000; Ayuso et al. 2016; Lode et al. 2017; Haroldson et al. 2018; Piercey and Kamber 2019; Gigon et al. 2020), therefore Pb isotope compositions of bulk minerals have been analyzed in many Te-bearing deposits in NE China. For example, the Pb isotope compositions of ore stage pyrite from the Te-bearing Yongxin and Tuanjiegou deposits plot in the range of Early Cretaceous intermediate to felsic rocks in the district (Appendix A Fig. A1), indicating that Pb in ore-forming fluids was leached from Early Cretaceous intermediate to felsic rocks or exsolved from corresponding magmas (Han 2013; Hao et al. 2016; Wang et al. 2016; Gao et al. 2017a; Li 2018; Zhai et al. 2018; Zhao et al. 2019b; Liu et al. 2019). However, the samples analyzed in this study have a range in Pb isotope compositions that indicate the source of Pb in ore-forming fluids are different for Te-rich and Te-poor epithermal Au-Ag deposits in NE China (Fig. 7a, b),

Always consult and cite the final, published document. See http:/www.minsocam.org or GeoscienceWorld

399 ranging from mafic or intermediate to felsic magmatic sources in each volcano-plutonic
400 center (Fig. 7c, d).

401 *Igneous sources*: In the Te-rich Sandaowanzi and Yongxin, and Te-poor Tuanjiegou
402 deposits the bulk Pb isotope compositions of main stage minerals are consistent with an
403 early Cretaceous magmatic source and are much less radiogenic than the underlying
404 basement (dashed pattern area; Fig. 7a, b; Appendix B Table B2). However, the in situ Pb
405 isotope compositions of ore minerals in these deposits are less radiogenic than their Early
406 Cretaceous intermediate-felsic host rocks and contemporaneous felsic igneous rocks
407 (blue line area) in the region (Fig. 7c, d). This shift implies that most of the less
408 radiogenic Pb in ore-forming fluids were not inherited from the host rocks or the regional
409 exposed contemporaneous intermediate to felsic rocks including andesite, dacite, tuff,
410 granite porphyry, and diorite. The less radiogenic Pb in ore-forming fluids must have
411 been derived from deeper intrusions with non-radiogenic Pb isotope compositions. This
412 trend is also similar to the Orcopampa epithermal Au-Ag deposit in Peru where Pb
413 isotopes from gold-rich stages are also less radiogenic than host rocks (Tosdal et al.
414 1999). This is also inferred for several other deposits elsewhere in the world (e.g.,
415 Porgera, Papua New Guinea; Orcopampa, Peru; Richards et al. 1991; Richards and Noble
416 1998; Bouse et al. 1999; Tosdal et al. 1999). We, therefore, infer that ore-forming fluids
417 for the three aforementioned deposits were derived from mafic intrusions at deeper levels
418 in the magmatic-hydrothermal systems.

Always consult and cite the final, published document. See http:/www.minsocam.org or GeoscienceWorld

Although Te and Au are compatible elements during mantle melting, they primarily reside in sulfides or discrete metallic phases (Patten et al. 2013; Jenner 2017). Consequently, the concentrations of S and Te in basaltic melts vary considerably with the proportion of metal-ligand in the reservoir (Helmy et al. 2020). For example, the highest Te concentrations occur when the ferrous iron cation is the principal metal-ligand (Helmy et al., 2020). Experiments show that major base metal sulfides do not balance the whole-rock Te concentrations of fertile mantle peridotites (Patten et al. 2013; Lorand and Luguet 2016). The missing Te fraction of the whole-rock budget (30–90%) was attributed to randomly distributed tellurides (Lorand and Alard 2010; Lorand and Luguet 2016). This can explain why Te is much less abundant (electrum [>95%] is the major gold- and silver-bearing mineral) than Au in Tuanjiegou. In this case, Te is controlled by dilution during extensive partial mantle melting.

In another Te-poor deposit (Dong'an), the Pb isotope compositions of ore minerals are slightly more radiogenic than the Early Cretaceous andesite and rhyolite (triangles outlined in green) in the region (Fig. 7c, d), but are similar to those of underlying Triassic to Jurassic intermediate-felsic igneous rocks (dashed line area; Fig. 7a, b) (e.g., Zhang et al. 2019). The geologic setting suggests that some of the radiogenic Pb in ore-forming fluids were leached from the Early Jurassic alkaline feldspar granite in the area. For example, the μ1 values in minerals (10.49 to 10.59) are higher than alkaline feldspar granite (μ1=10.40 with the age of 176 Ma; Zhi et al., 2016). However, the presence of late-stage fluorite in the veins suggests that fluorine was derived from a more fractionated

Always consult and cite the final, published document. See http:/www.minsocam.org or GeoscienceWorld

and crustally contaminated early Cretaceous F-rich porphyry intrusion (Li et al. 2014, 2019). Therefore, the ore-forming fluids at Dong'an were likely discharged from an Early Cretaceous intermediate-felsic intrusion (Pb median=14.7 ppm; Zhang et al., 2010) that obtained most of its Pb from underlying Jurassic felsic igneous rocks with a median of 13.2 ppm Pb (Zhi et al., 2016) in the region.

Country rock sources: Country rock contamination is common in mafic-derived Au-Ag deposits, but generally results in very small shifts (e.g., $^{206}Pb/^{204}Pb$ ~0.05; Richards et al. 1991; Tosdal et al. 1999). In general, bulk Pb isotope data from sulfides (e.g., pyrite) have a large range, such as $^{206}Pb/^{204}Pb$ from 18.17 to 18.37 in the Tuanjiegou deposit. The in situ Pb isotope data presented in this study more clearly show country rock contamination than the bulk Pb isotope data generated by previous workers. The generally low Pb concentrations of ore-stage minerals as well as their small Pb isotope variations suggest that the contribution of Pb from the host rocks was minimal until the hydrothermal fluid was depleted of Pb (Tosdal et al. 1999). For example, the radiogenic Pb isotope compositions of altaite, petzite, and sylvanite at Sandaowanzi extend towards the Cambrian metasedimentary and Ordovician igneous rock trend. Yongxin is shifted slightly towards this trend (Fig. 7e, f). Dong'an extends from the Triassic-Jurassic rock trend towards the Cambrian-Ordovician rock trend. These shifts suggest that ore-forming fluids dissolved Pb as they flowed through underlying metasedimentary and igneous rocks of different ages, and therefore contain multi-stage

Always consult and cite the final, published document. See http:/www.minsocam.org or GeoscienceWorld

460 lead (Richards et al. 1991; Tosdal et al. 1999). To further evaluate the lead sources,
461 evolution models were calculated.
462
463 **5.1.2. Lead isotope evolution models**
464
465 All of the in situ Pb isotope data obtained on ore minerals in in this study have linear
466 distributions. Although these linear data arrays do not yield meaningful isochron ages,
467 they provide evidence of mixing between Pb sources (e.g., Harolson et al. 2018; Gigon et
468 al. 2020). To advance understanding of the Pb sources in these deposits, a Pb isotope
469 evolution model was built. The model assumes that the crustal Pb involved in
470 crust-mantle mixing has undergone a two-stage evolution process (Stacey and Kramers
471 1975). The model age of both Pb sources is based on the maximum and minimum ages
472 for each deposit (Table 6). The parameters for the model are $\mu1_{max}$ and $\mu1_{min}$ which are
473 the $^{238}U/^{204}Pb$ ratio for the lead sources 1 and 2 respectively, and $t1_{max}$ and $t1_{min}$ the
474 timings of crust formation for lead sources 1 and 2 respectively. Max and Min are the
475 maximum and minimum data from each deposit. Back-calculation indicates the
476 extraction of a crustal reservoir from the mantle at $t1_{max}$ Ga that evolved toward the
477 composition of Pb source 1 ($\mu1_{max}$), followed at $t1_{min}$ Ga by the extraction of another
478 crustal reservoir from the mantle that evolved toward the composition of Pb source 2
479 ($\mu1_{min}$) in each deposit. The Pb isotope model is shown in Figure 8. Low μ1 values
480 indicate that Pb was likely derived from mafic magmas (Tosdal et al. 1999), whereas high

Always consult and cite the final, published document. See http:/www.minsocam.org or GeoscienceWorld

481 μ1 values suggest that Pb was derived from more crustally contaminated felsic magmas
482 (Gigon et al. 2020).

483 Tellurium-rich deposits have low μ1 values. For example, Yongxin has the lowest μ1
484 values (9.14 to 9.15) and Sandaowanzi (9.41 to 9.42) have slightly higher μ1 values. In
485 contrast, μ1 values are much higher in the Te-poor Dong'an deposit (10.49 to 10.59). In
486 addition, Tuanjiegou (9.41 to 9.44) has low μ1 values, but Te is poor. This is explained
487 by Te dilution during mantle melting as mentioned above. In this case, Te was not
488 transported to shallow levels (<2 km) with Au. Although both Te-rich and Te-poor
489 deposits have mixed Pb sources, Pb in Te-bearing fluids may be from a non-radiogenic
490 source in the region.

491 Compared with other Te-rich systems, such as intrusion-related systems in the
492 margin of the North China Craton, non-radiogenic Pb sources are common (e.g.,
493 Dongping and Dabaiyang; Zhang and Mao 1995; Shen et al. 2020). Those deposits are
494 related to alkaline intrusions which are likely from a mantle source (e.g., Mao et al. 2003;
495 Gao et al. 2017b). In other gold-rich systems in the North China Craton, radiogenic Pb
496 sources are common and are related to basement contributions (e.g., Sidaogou in
497 Liaodong in the northeast; Feng et al. 2019). Thus, in both epithermal and
498 intrusion-related systems, Te is related to non-radiogenic Pb sources, but Au has both
499 mantle and basement contributions.

500

501 **5.2. Noble gas isotopes and fluid inclusion microthermometry**

Always consult and cite the final, published document. See http:/www.minsocam.org or GeoscienceWorld

This is the peer-reviewed, final accepted version for American Mineralogist, published by the Mineralogical Society of America.
The published version is subject to change. Cite as Authors (Year) Title. American Mineralogist, in press.
DOI: https://doi.org/10.2138/am-2022-8552. http://www.minsocam.org/

502

503 **5.2.1. Noble gas sources**

504

505 The proportion of atmospheric, crustal, and mantle He, Ne, and Ar trapped in ore and
506 gangue minerals from the Sandaowanzi, Yongxin, Dong'an, and Tuanjiegou deposits was
507 determined to elucidate the source(s) of volatiles in the magmatic-hydrothermal systems.
508 Twenty new data sets (He, Ne, and Ar; Table 5) supplement twenty-one published data
509 sets (He and Ar only; Appendix B Table B3; Yu et al. 2012; Zhai et al. 2015; Li 2018; He
510 et al., 2023). To determine the source of volatiles in these epithermal deposits, He, Ne,
511 and Ar isotopic data are plotted on Figure 9 relative to the isotopic composition of air,
512 crust, and mantle, geothermal water in the Basin and Range province and Cascades arc in
513 the western U.S. (Fig. 9c and d only), as well as hydrothermal gold deposits related to
514 subduction of the Paleo-Pacific Ocean in East China (e.g., intrusion-related deposits; Tan
515 et al., 2018) and South Korea (epithermal deposits; Kim et al., 2012) during the Early to
516 Late Cretaceous. In magmatic-hydrothermal systems (e.g., epithermal deposits in South
517 Korea and western U.S.), the large range of He ratios, and in some cases Ne and Ar
518 isotope ratios, have been interpreted to reflect mixing between air saturated meteoric
519 water, meteoric groundwater that obtained radiogenic crustal helium from older country
520 rocks, and mantle-derived magmatic fluids (e.g., Kim et al., 2012; Manning and Hofstra
521 2017 and references therein).

522 The samples investigated in this study have lower R/R_A than geothermal sites from

Always consult and cite the final, published document. See http:/www.minsocam.org or GeoscienceWorld

the Cascades arc and overlap those in the Basin and Range (B&R) province and Late Cretaceous epithermal deposits in South Korea (Fig. 9c, d; Kennedy and van Soest 2007), but are unlike intrusion-related systems in China (Appendix B Table B3). This result indicates that epithermal deposits in the Early Cretaceous magmatic arc in NE China formed from fluids containing a smaller proportion of mantle helium than geothermal sites in the Cascades arc and Late Cretaceous epithermal deposits in South Korea. This is likely due to a greater proportion of meteoric water as in geothermal sites in the Basin and Range province and NE China. At Sandaowanzi, data from barren quartz and pyrite plot between air and crust (Fig. 9c–e), whereas data from ore stage petzite and chalcopyrite plot between crust and mantle (Fig. 9c). These trends reflect mixing between magmatic fluids with mantle ^{3}He and air-saturated meteoric groundwater with variable amounts of crustal ^{4}He. At Yongxin, main stage pyrite has high ^{4}He concentrations, R/R_A ratios and $^{20}Ne/^{22}Ne$ ratios, as well as low $CO_2/^{3}He$ ratios (Fig. 9a, b, e), indicating that ore stage fluids contained mantle-derived volatiles. At Dong'an, later quartz and fluorite also have high R/R_A and $^{20}Ne/^{22}Ne$ (Fig. 9a–e). These results reflect mixing among air saturated meteoric water with variable amounts of crustal ^{4}He and magmatic fluids with mantle ^{3}He. At Tuanjiegou, quartz and late calcite plot between air and crust (Fig. 9c, d). Ore stage pyrite has high $CO_2/^{3}He$ ratios and low ^{4}He and variable $^{20}Ne/^{22}Ne$ ratios (Fig. 9a, b, e). This result is indicative of mixing between air saturated meteoric water with variable amounts of crustal ^{4}He, anomalous CO_2 and a small amount of magmatic fluid with mantle ^{20}Ne.

Always consult and cite the final, published document. See http:/www.minsocam.org or GeoscienceWorld

In this study, main stage minerals (tellurides, chalcopyrite, telluride-bearing pyrite, fluorite, adularia, quartz) in both Te-rich and Te-poor deposits have a greater portion of mantle helium (1–25%) than early- and late-ore stage minerals (quartz, adularia, calcite, barren pyrite) (Fig. 9a–d). Notably, main stage tellurides and chalcopyrite in the Te-rich Sandaowanzi deposit have 1–15% mantle helium and telluride-bearing pyrite from Yongxin has 10–25% mantle helium (Fig. 9c, d). The samples with more mantle helium also have more mantle neon (Fig. 9e), which is consistent with a mafic magmatic source (Hofstra et al. 2016). In contrast, Te-poor deposits have lower proportions of mantle helium (Fig. 9a, b), such as 1–5% mantle helium at Dong'an (Fig. 9c, d), which is likely due to dilution by voluminous meteoric water as in many other classic epithermal systems (O'Neil and Silberman 1974; Hedenquist and Lowenstern 1994; Cooke and Simmons 2000; Simmons et al. 2005, 2016; Manning and Hofstra 2017). Pyrite from the Tuanjiegou deposit has 1–15% mantle helium but is Te-poor due to Te dilution during partial mantle melting (Patten et al. 2013; Lorand and Luguet, 2016; Jenner 2017).

Low R/R_A ratios indicative of crustal sources are common in epithermal Au-Ag systems (e.g., Manning and Hofstra 2017). In this study, the proportion of crustal helium is highest in early- and late-stage minerals, especially early-stage pyrite in altered host rocks (Fig. 9a–d) at Sandaowanzi and Dong'an (Yu et al. 2012; Zhai et al. 2015 and reference therein). Noble gas isotopes show that early-barren pyrites contain crustal helium ($He_{(mantle)} < 1\%$). The proportion of crustal helium is also large in early-quartz veins at Yongxin and Tuanjiegou ($He_{(mantle)} = \sim 1\%$). Some of the early- and late-stage

Always consult and cite the final, published document. See http:/www.minsocam.org or GeoscienceWorld

565 minerals have isotopic compositions that plot on or near the mixing line between air and
566 crust (Fig. 9c–e). These compositions are characteristic of air saturated meteoric water
567 that convected through old rocks containing radiogenic ^{4}He (Manning and Hofstra 2017).
568 Generally, these fluids are not important sources of precious metals.

569 Epithermal deposits have higher ^{20}Ne, ^{36}Ar, and ^{4}He than intrusion-related deposits
570 due to shallow levels (<2 km) with a high proportion of noble gas isotope from air (Fig.
571 9c–e). Low-sulfidation deposits in South Korea have lower ^{4}He and higher R/R_A than
572 epithermal deposits in NE China. This trend indicates that the Late Cretaceous epithermal
573 deposits in South Korea have a large mantle contribution. In intrusion-related systems in
574 the margin of the North China Craton, Jibei in the north has more mantle He (from ~10%
575 to ~75%) than Jiaodong (from ~1% to ~50%) in the east, Liaodong (from ~1% to ~30%)
576 in the northeast, and Xiaoqing (from ~1% to ~30%) in the south. The greater proportion
577 of mantle He (~75%) is consistent with less radiogenic Pb and indicates that the Te-rich
578 epithermal deposits formed in magmatic-hydrothermal systems with significant
579 contributions of mantle-derived volatiles (e.g., Dongping; Mao et al. 2003; Gao et al.
580 2015, 2017b).

581

582 **5.2.2. Fluid evolution**

583

584 The crustal signature of deeply circulated meteoric ground water in early- and
585 late-stage minerals (Fig. 9c, d) may be caused by water-rock reaction along fluid flow

Always consult and cite the final, published document. See http:/www.minsocam.org or GeoscienceWorld

586 paths as evident in other epithermal systems (O'Neil and Silberman 1974; Hedenquist and
587 Lowenstern 1994; Simmons 1995; Simmons et al. 2005). Evidence of magmatic inputs
588 into hydrothermal fluids is clearer in the main stage minerals of Te-rich deposits (Fig. 9c,
589 d), although these fluids were also diluted by meteoric water (O'Neil and Silberman 1974;
590 Hedenquist and Lowenstern 1994; Simmons et al. 2005, 2016; Manning and Hofstra
591 2017; Gao et al. 2021). The trends in Figure 9c, d are interpreted to result from input of
592 magmatic fluid with mantle He into variably exchanged meteoric ground water with
593 crustal He (e.g., Manning and Hofstra 2017). Despite the predominance of meteoric water
594 at shallow levels (<2 km), Te- and Au-related minerals still contain a relatively large
595 proportion of mantle-derived components (up to ~9 R/R_A; Simmons et al. 1987; Kim et
596 al., 2012; Mao et al. 2003; Saunders et al. 2008; Manning and Hofstra 2017).

597 In the epithermal systems studied, ore-forming fluids have low temperatures and
598 salinities (<5%; Fig. 10). However, inputs of higher salinity fluids (~5–10%) are evident
599 in the Te-rich Au deposits. Although noble gas data have a large range of R/R_A, Te-rich
600 systems usually have higher proportions of mantle-derived volatiles. The Te-rich
601 Yongxin deposit has the highest salinities and the highest temperature and proportion of
602 mantle He, which are indicative of mafic magma contributions (Fig. 10). The Te-rich
603 Sandaowanzi and Te-poor Tuanjiegou deposits have a few samples with high salinity
604 inclusions, which is likely related to periodic inputs of magmatic fluids. The Te-poor
605 Dong'an deposit has low salinities with various temperatures indicative of a meteoric
606 water dominant system. This interpretation is supported by recent secondary ion mass

Always consult and cite the final, published document. See http:/www.minsocam.org or GeoscienceWorld

607 spectroscopy (SIMS) oxygen isotope evidence (Gao et al. 2021). Thus, input of magmatic
608 fluids with a mantle source and moderately high salinity (e.g., >5%) are characteristic of
609 Te-rich epithermal Au systems. The Te-rich deposits have high salinity, possibly because
610 Te is carried as a chloride complex (e.g., Cook et al., 2023).
611
612 **5.3. Conclusions**
613
614 Integrated geologic, in situ Pb isotopic, noble gas isotope, and fluid inclusion
615 microthermometry evidence were used to construct a fluid source and evolution model
616 for the epithermal Au-Ag deposits in the north Heilongjiang province in NE China (Fig.
617 11). The Pb, noble gas isotope, and fluid inclusion microthermometry results indicate that
618 Te-rich epithermal deposits likely formed from fluids discharged from mafic intrusions
619 underlying northern Heilongjiang province.
620 In the model, Te-rich epithermal deposits are located along the Nenjiang-Heihe fault
621 near the margin of the Xing'an Block. The Te-rich veins are exposed at different depths
622 as Sandaowanzi is hosted by Early Cretaceous calc-alkaline andesite or dacite (e.g., Liu
623 et al. 2011; Gao et al. 2017a, 2018a) and Yongxin is hosted in the contact zone of Early
624 Cretaceous andesite and Triassic mylonite (e.g., Li 2018; Zhao et al. 2019a). Ore stage
625 minerals have the least radiogenic Pb isotope compositions ($^{206}Pb/^{204}Pb$ from 18.1 to 18.3)
626 in both deposits. These values are also lower than the intermediate to felsic host rocks.
627 The Pb isotope model shows that ore minerals have low μ1 values (down to 9.14). These

Always consult and cite the final, published document. See http:/www.minsocam.org or GeoscienceWorld

628 results suggest that ore-forming fluids were likely derived from deeper mafic intrusions.
629 Noble gas evidence shows that ore stage tellurides, chalcopyrite and pyrite contain more
630 mantle helium (up to 25%) than early- and late-stage minerals (~1%) (Yu et al. 2012;
631 Zhai et al. 2015 and reference therein). A large proportion of mantle He in fluids is also
632 evident in the deeper Te- and Bi-rich intrusion-related Dongping deposit in north China
633 (Mao et al. 2003), and in the Te-rich adularia-sericite epithermal Au-Ag deposits in South
634 Korea (Kim et al. 2012). These fluids are moderately saline (>~5 eq. wt. % NaCl; Fig.
635 10). Thus, productive high-grade Au-Ag-telluride ores in adularia-sericite epithermal
636 systems may form by the input of magmatic fluids with mantle-derived volatiles from
637 concealed mafic intrusions into barren meteoric flow systems (e.g., Gao et al. 2021).

638 Tellurium-poor deposits such as Dong'an in the Songliao Block and Tuanjiegou in
639 the Jiamusi Massif are hosted by Early Cretaceous rhyolite and Early Jurassic granite
640 (e.g., Zhang et al. 2010) and Early Cretaceous granodiorite porphyry (Sun et al. 2013;
641 Wang et al. 2016; White et al. 2019), respectively. Ore stage minerals at Dong'an have
642 the most radiogenic Pb isotope compositions ($^{206}Pb/^{204}Pb$ from 18.8 to 18.9) and the
643 highest μ1 values (up to 10.54). These data imply that the ore-forming fluids were likely
644 derived from crustally contaminated intermediate to felsic magmas. Although Tuanjiegou
645 has a non-radiogenic Pb isotope composition consistent with a mafic magma source, Te is
646 much less abundant (electrum [>95%] is the major gold- and silver-bearing mineral) than
647 Au, which is controlled by Te-poor magmatic systems. These features are similar to those
648 of most adularia-sericite epithermal Au-Ag deposits in the world (O'Neil and Silberman

Always consult and cite the final, published document. See http:/www.minsocam.org or GeoscienceWorld

This is the peer-reviewed, final accepted version for American Mineralogist, published by the Mineralogical Society of America.
The published version is subject to change. Cite as Authors (Year) Title. American Mineralogist, in press.
DOI: https://doi.org/10.2138/am-2022-8552. http://www.minsocam.org/

649 1974; Hedenquist and Lowenstern 1994; Cooke and Simmons 2000; Simmons et al. 2005;
650 Manning and Hofstra 2017; John et al. 2003a, b, 2018; White et al. 2019).
651
652 **6. Implications**
653
654 The in situ *fs*LA-MC-ICP-MS Pb isotope analyses of tellurides, coexisting sulfides
655 and hydrothermal minerals with various beam sizes (5–75 μm) presented herein are the
656 first to be conducted in Te-bearing epithermal Au deposits. The Pb isotopic results show
657 that Te-rich epithermal deposits have the least radiogenic Pb isotope compositions and
658 the lowest μ1 values indicative of a mafic source. The Te-poor epithermal deposits are
659 controlled by Te-poor magmatic systems or dominated by meteoric ground water that
660 contain smaller proportion of mantle helium. These conclusions are also supported by
661 noble gas (He, Ne, and Ar) isotopic composition of fluid inclusion extracts from various
662 ore and gangue minerals and fluid inclusion microthermometry. For example, Te-rich
663 Yongxin deposits have a larger proportion of mantle helium up to 25%, providing clear
664 evidence for mafic magmatic sources.
665 This study demonstrates that in situ Pb isotope compositions obtained from Au-, Ag-,
666 and Te-bearing minerals can be used to constrain the source of critical and precious
667 metals in hydrothermal deposits. Together, the Pb, noble gas isotope compositions, and
668 fluid inclusion microthermometry show that the Te-rich epithermal deposits in NE China
669 are associated with special volcano-plutonic centers, where ore-forming fluids in

Always consult and cite the final, published document. See http:/www.minsocam.org or GeoscienceWorld

670 mantle-derived mafic magmas were discharged into convecting meteoric water. The
671 volcano-plutonic centers with the least radiogenic Pb isotope compositions ($^{206}Pb/^{204}Pb <$
672 18.3) have the greatest potential for Te-rich epithermal Au-Ag deposits in NE China, and
673 perhaps elsewhere.

674 In future studies, Pb isotopes together with Te stable isotopes using MC-ICP-MS
675 (e.g., Fehr et al., 2004) have the potential to constrain both Te and Au sources in
676 hydrothermal systems. However, Te isotopes on Au-Ag-Te minerals and native Te in ore
677 deposits have relatively large Te isotope variations (Fornadel et al. 2014; 2017). At
678 present, the processes responsible for those variations are unclear, although few studies
679 have been conducted on tellurides from ore deposits (Fornadel et al. 2019). Thus, before
680 the Te isotope system can be applied to ore-forming systems, such as those in NE China,
681 more laboratory studies could help identify the cause of the large Te isotope variations
682 obtained thus far.

683

684 **Acknowledgements**

685

686 The authors are grateful to the Bureau of Geology and Mineral Exploration
687 (Heilongjiang), the Geological Brigades of the Heilongjiang Geological Survey, and
688 Sandaowanzi, Dong'an and Tuanjiegou Gold Co. Ltd. for their support of the field work.
689 The manuscript benefited from reviews by Dr. Stephan Schuth, Associated Editor Dr.
690 Daniel Gregory, and the U.S. Geological Survey reviewer Dr. Nora K. Foley. This study

Always consult and cite the final, published document. See http:/www.minsocam.org or GeoscienceWorld

691 was funded by the National Natural Science Foundation of China (Grant Nos. 42272080
692 and 41802099), the Major Research Plan of National Natural Science Foundation of
693 China (Grant No. 92062219), the Second Tibetan Plateau Scientific Expedition and
694 Research Program (STEP, Grant No. 2019QZKK0806), and the Fundamental Research
695 Funds for the Central Universities (Grant No. 2-9-2021-021). Any use of trade, firm, or
696 product names is for descriptive purposes only and does not imply endorsement by the
697 U.S. Government.

698

699 **References**

700

701 Albrecht M, Derrey IT, Horn I, Schuth S and Weyer S (2014) Quantification of trace
702 element contents in frozen fluid inclusions by UV-fs-LA-ICP-MS analysis. Journal
703 of Analytical Atomic Spectrometry 29: 1034-1041.

704 Ayuso RA, Slack JF, Day WC and McCafferty AE (2016) Geochemistry, Nd-Pb isotopes,
705 and Pb-Pb ages of the Mesoproterozoic Pea Ridge iron oxide-apatite–rare earth
706 element deposit, southeast Missouri. Economic Geology 111: 1935-1962.

707 Bouse RM, Ruiz J, Titley SR, Tosdal RM and Wooden JL (1999) Lead isotope
708 compositions of Late Cretaceous and early Tertiary igneous rocks and sulfide
709 minerals in Arizona; implications for the sources of plutons and metals in porphyry
710 copper deposits. Economic Geology 94: 211-244.

711 Ciobanu CL, Cook NJ and Spry PG (2006) Preface – Special Issue: Telluride and

Always consult and cite the final, published document. See http:/www.minsocam.org or GeoscienceWorld

This is the peer-reviewed, final accepted version for American Mineralogist, published by the Mineralogical Society of America.
The published version is subject to change. Cite as Authors (Year) Title. American Mineralogist, in press.
DOI: https://doi.org/10.2138/am-2022-8552. http://www.minsocam.org/

712 selenide minerals in gold deposits – how and why. Mineralogy and Petrology 87:
713 163-169.

714 Cook NJ, Ciobanu CL, Spry PG and Voudouris P (2009) Understanding
715 gold-(silver)-telluride-(selenide) mineral deposits. Episodes 32: 249-263.

716 Cook DA, Reeves SJ, Zhang W, Reid G, Levason W, Bartlett PN, Dyke JM, Greenacre
717 VK (2023) Tellurium electrodeposition from tellurium (II) and (IV) chloride salts in
718 dichloromethane. Electrochimica Acta 456: 142456.

719 Cooke DR and Simmons SF (2000) Characteristics and Genesis of Epithermal Gold
720 Deposits, in Hagemann, SG and Brown PE (Eds.), Gold in 2000. Society of
721 Economic Geologists Inc., pp 221-244.

722 Ding RX, Shu P, Ji XY, Qu YM, Chen RH and Zhang B (2007) SHRIMP zircon U-Pb age
723 and geological meaning of reservoir volcanic rocks in Qingshen gas field of the
724 Songliao Basin, NE China. Journal of Jilin University (Earth Science Edition) 37:
725 525-530 (in Chinese with English abstract).

726 Fehr MA, Rehkämper M and Halliday AN (2004) Application of MC-ICPMS to the
727 precise determination of tellurium isotope compositions in chondrites, iron
728 meteorites and sulfides. International Journal of Mass Spectrometry 232: 83-94.

729 Feng H, Shen P, Zhu R, Li C, Ma G and Pan H (2019) Geology and He-Ar-S-Pb isotope
730 constraints on the genesis of the Sidaogou gold deposit in Liaodong Peninsula,
731 northeastern North China Craton. Ore Geology Reviews 113: 103080.

732 Foley NK and Ayuso RA (1994) Lead isotope compositions as guides to early gold

Always consult and cite the final, published document. See http:/www.minsocam.org or GeoscienceWorld

This is the peer-reviewed, final accepted version for American Mineralogist, published by the Mineralogical Society of America.
The published version is subject to change. Cite as Authors (Year) Title. American Mineralogist, in press.
DOI: https://doi.org/10.2138/am-2022-8552. http://www.minsocam.org/

733 mineralizations; the North Amethyst vein system, Creede District, Colorado.
734 Economic Geology 89: 1842-1859.
735 Fornadel AP, Spry PG and Jackson SE (2019) Geological controls on the stable tellurium
736 isotope variation in tellurides and native tellurium from epithermal and orogenic gold
737 deposits: Application to the Emperor gold-telluride deposit, Fiji. Ore Geology
738 Reviews 113: 103076.
739 Fornadel AP, Spry PG, Haghnegahdar MA, Schauble EA, Jackson SE and Mills SJ (2017)
740 Stable Te isotope fractionation in tellurium-bearing minerals from precious metal
741 hydrothermal ore deposits. Geochimica et Cosmochimica Acta 202: 215-230.
742 Fornadel AP, Spry PG, Jackson SE, Mathur RD, Chapman JB and Girard I (2014)
743 Methods for the determination of stable Te isotopes of minerals in the system
744 Au-Ag-Te by MC-ICP-MS. Journal of Analytical Atomic Spectrometry 29: 623-637.
745 Galer SJG and Abouchami W (1998) Practical application of lead triple spiking for
746 correction of instrumental mass discrimination. Mineralogical Magazine 62A:
747 491-492.
748 Gao FH, Xu WL, Yang DB, Pei FP, Liu XM and Hu ZC (2007) LA-ICP-MS zircon U-Pb
749 dating from granitoids in southern basement of Songliao basin: constraints on ages of
750 the basin basement. Science in China (Series D) 50: 995-1004.
751 Gao S (2017) Study on Mesozoic gold metallogenic system, northern Heihe,
752 Heilongjiang province. PhD thesis, Beijing, China, China University of Geosciences
753 (Beijing), pp 1-196 (in Chinese with English abstract).

Always consult and cite the final, published document. See http:/www.minsocam.org or GeoscienceWorld

This is the peer-reviewed, final accepted version for American Mineralogist, published by the Mineralogical Society of America.
The published version is subject to change. Cite as Authors (Year) Title. American Mineralogist, in press.
DOI: https://doi.org/10.2138/am-2022-8552. http://www.minsocam.org/

754 Gao S, Hofstra AH, Qin K and Xu H (2022) A case of Te-rich low-sulfidation epithermal
755 Au-Ag deposits in a calc-alkaline magmatic arc, NE China. Ore Geology Reviews
756 115: 105158.
757 Gao S, Hofstra AH, Zou X, Valley JW, Kitajima K, Marsh EE, Lowers HA, Adams DT,
758 Qin K and Xu H (2021) Oxygen isotope evidence for input of magmatic fluids and
759 precipitation of Au-Ag-tellurides in an otherwise ordinary adularia-sericite
760 epithermal system in NE China. American Mineralogist 106: 2003-2019.
761 Gao S, Xu H, Li SR, Santosh M, Zhang DS, Yang LJ and Quan SL (2017b) Hydrothermal
762 alteration and ore-forming fluids associated with gold-tellurium mineralization in the
763 Dongping gold deposit, China. Ore Geology Reviews 80: 166-184.
764 Gao S, Xu H, Quan SL, Zang YQ and Wang T (2018b) Geology, hydrothermal fluids,
765 H-O-S-Pb isotopes, and Rb-Sr geochronology of the Daxintun orogenic gold deposit
766 in Heilongjiang province, NE China. Ore Geology Reviews 92: 569-587.
767 Gao S, Xu H, Zang YQ and Wang T (2018a) Mineralogy, ore-forming fluids and
768 geochronology of the Shangmachang and Beidagou gold deposits, Heilongjiang
769 province, NE China. Journal of Geochemical Exploration 188: 137-155.
770 Gao S, Xu H, Zang YQ, Yang LJ, Yang B and Wang T (2017a) Late Mesozoic
771 magmatism and metallogeny in NE China: The Sandaowanzi-Beidagou example.
772 International Geology Review 59: 1413-1438.
773 Gao S, Xu H, Zhang DS, Shao HN and Quan SL (2015) Ore petrography and chemistry
774 of the tellurides from the Dongping gold deposit, Hebei Province, China. Ore

Always consult and cite the final, published document. See http:/www.minsocam.org or GeoscienceWorld

This is the peer-reviewed, final accepted version for American Mineralogist, published by the Mineralogical Society of America.
The published version is subject to change. Cite as Authors (Year) Title. American Mineralogist, in press.
DOI: https://doi.org/10.2138/am-2022-8552. http://www.minsocam.org/

775 Geology Reviews 64: 23-34.

776 Ge WC, Wu FY, Zhou CY and Zhang JH (2005) Zircon U-Pb ages and its significance of
777 the Mesozoic granites in the Wulanhaote Region, central Great Xing'an Range. Acta
778 Petrologica Sinica 21: 749-762 (in Chinese with English abstract).

779 Gigon J, Deloule E, Mercadier J, Huston DL, Richard A, Annesley IR, Wygralak AS,
780 Skirrow RG, Mernagh TP and Masterman K (2020) Tracing metal sources for the
781 giant McArthur River Zn-Pb deposit (Australia) using lead isotopes. Geology 48:
782 478-482.

783 Goldfarb RJ, Berger BR, George MW and Seal RR, II (2017) Tellurium, in Schulz KJ,
784 DeYoung JH, Jr Seal RR II and Bradley DC (Eds.), Critical Mineral Resources of the
785 United States—Economic and Environmental Geology and Prospects for Future
786 Supply US Geological Survey Professional Paper 1802, R1-R27.

787 Goldfarb RJ, Hofstra AH and Simmons SF (2016) Critical elements in Carlin, epithermal,
788 and orogenic gold deposits, in Verplanck PL and Hitzman MW (Eds.), Rare Earth
789 and Critical Elements in Ore Deposits. Society of Economic Geologists Inc., pp
790 217-244.

791 Graham DW (2002) Noble gas isotope geochemistry of mid-ocean ridge and ocean island
792 basalts: characterization of mantle source reservoirs, in Porcelli D, Ballentine CJ and
793 Wieler R (Eds.), Reviews in Mineralogy and Geochemistry, Noble Gases in
794 Geochemistry and Cosmochemistry, vol. 47. Mineralogical Society of America,
795 Washington, D.C., pp 247-318.

Always consult and cite the final, published document. See http:/www.minsocam.org or GeoscienceWorld

This is the peer-reviewed, final accepted version for American Mineralogist, published by the Mineralogical Society of America.
The published version is subject to change. Cite as Authors (Year) Title. American Mineralogist, in press.
DOI: https://doi.org/10.2138/am-2022-8552. http://www.minsocam.org/

796 Gulson BL (1986) Lead isotope in mineral exploration. Developments in Economic
797 Geology Series, Elsevier, pp 245.
798 Hall DL, Sterner SM and Bodnar RJ (1988) Freezing point depression of NaCl-KCl-H_2O
799 solutions. Economic Geology 83: 197-202.
800 Han S (2013) Magmatic fluids and gold mineralization of the late Mesozoic epithermal
801 gold system in northern Lesser Xing'an Range, NE China. PhD thesis, Changchun,
802 China, Jilin University, pp 47-50 (in Chinese with English abstract).
803 Hao B, Deng J, Bagas L, Ge L, Nie F, Turner S, and Qing M (2016) The Gaosongshan
804 epithermal gold deposit in the Lesser Hinggan Range of the Heilongjiang Province,
805 NE China: implications for Early Cretaceous mineralization. Ore Geology Reviews
806 73: 179-197.
807 Haroldson EL, Beard BL, Satkoski AM, Brown PE and Johnson CM (2018) Gold
808 remobilization associated with Mississippi Valley–type fluids: A Pb isotope
809 perspective. Geological Society of America Bulletin 130: 1583-1595.
810 He J, Liu J, Li X, Wang X and Sun P (2023) Genesis of Tuanjiegou epithermal gold
811 deposit in Heilongjiang province: Zircon U-Pb dating, element geochemistry and
812 Hf-S-Pb-He isotopic evidence. Journal to Jilin University (Earth Science Edition),
813 doi: 10.13278/j.cnki.jjuese.20210387 (in Chinese with English abstract).
814 Hedenquist JW and Lowenstern JB (1994) The role of magmas in the formation of
815 hydrothermal ore deposits. Nature 370: 519-527.
816 Helmy HM, Ballhaus C, Fonseca RO and Leitzke FP (2020) Concentrations of Pt, Pd, S,

Always consult and cite the final, published document. See http:/www.minsocam.org or GeoscienceWorld

This is the peer-reviewed, final accepted version for American Mineralogist, published by the Mineralogical Society of America.
The published version is subject to change. Cite as Authors (Year) Title. American Mineralogist, in press.
DOI: https://doi.org/10.2138/am-2022-8552. http://www.minsocam.org/

As, Se and Te in silicate melts at sulfide, arsenide, selenide and telluride saturation: Evidence of PGE complexing in silicate melts? Contributions to Mineralogy and Petrology 175: 1-14.

Hilton DR, Fischer TP and Marty B (2002) Noble gases and volatile recycling at subduction zones, in Porcelli D, Ballentine CJ and Wieler R (Eds.), Reviews in Mineralogy and Geochemistry, Noble Gases in Geochemistry and Cosmochemistry, vol. 47. Mineralogical Society of America, Washington, D.C., pp 319-370.

Hofstra AH and Cline JS (2000) Characteristics and models for Carlin-type gold deposits, in Hagemann SG and Brown PE (Eds.), Gold in 2000. Society of Economic Geologists Inc., pp 163-220.

Hofstra AH, Meighan CJ, Song X, Samson I, Marsh EE, Lowers HA, Emsbo P and Hunt AG (2016) Mineral thermometry and fluid inclusion studies of the Pea Ridge iron oxide-apatite–rare earth element deposit, Mesoproterozoic St Francois Mountains terrane, southeast Missouri, USA. Economic Geology 111: 1985-2016.

Holwell DA, Fiorentini M, McDonald I, Lu Y, Giuliani A, Smith DJ, Keith M and Locmelis M (2019) A metasomatized lithospheric mantle control on the metallogenic signature of post-subduction magmatism. Nature Communications 10: 3511.

Jahn BM (2004) The Central Asian Orogenic Belt and growth of the continental crust in the Phanerozoic, in Malpas J, Fletcher CJN, Ali JR and Aitchison JC (Eds), Aspects of the Tectonic Evolution of China. Special Publication 226: 73-100.

Jahn BM, Wu FY and Chen B (2000) Massive granitoids generation in central Asia: Nd

Always consult and cite the final, published document. See http:/www.minsocam.org or GeoscienceWorld

This is the peer-reviewed, final accepted version for American Mineralogist, published by the Mineralogical Society of America.
The published version is subject to change. Cite as Authors (Year) Title. American Mineralogist, in press.
DOI: https://doi.org/10.2138/am-2022-8552. http://www.minsocam.org/

838 isotopic evidence and implication for continental growth in the Phanerozoic.
839 Episodes 23: 82-92.

840 Jenkin GRT, Graham H, Smith DJ, Khan R, Abbott AP, Harris RC, Holwell DA, Graham
841 SD, Khan R and Stanley CJ (2019) Gold and critical element recovery with
842 environmentally benign Deep Eutectic Solvents. 15th SGA Biennial Meeting abstract
843 4: 1512-1515.

844 Jenner FE (2017) Cumulate causes for the low contents of sulfide-loving elements in the
845 continental crust. Nature Geoscience 10: 524-529.

846 Jensen EP and Barton MD (2000) Gold deposits related to alkaline magmatism, in
847 Hagemann SG and Brown PE (Eds.), Gold in 2000. Society of Economic Geologists
848 Inc., pp 279-314.

849 John DA, Hofstra AH and Theodore TG (2003b) A special issue devoted to gold deposits
850 in northern Nevada: Part 1 regional studies and epithermal deposits. Economic
851 Geology 98: 225-234.

852 John DA, Hofstra AH, Fleck RJ, Brummer JE and Saderholm EC (2003a) Geologic
853 setting and genesis of the Mule Canyon low-sulfidation epithermal gold-silver
854 deposit, North-Central Nevada. Economic Geology 98: 425-463.

855 John DA, Vikre PG, du Bray EA, Blakely RJ, Fey DL, Rockwell BW, Mauk JL,
856 Anderson ED and Graybeal FT (2018) Descriptive models for epithermal gold-silver
857 deposits: US Geological Survey Scientific Investigations Report 2010–5070–Q, pp
858 7-12.

Always consult and cite the final, published document. See http:/www.minsocam.org or GeoscienceWorld

This is the peer-reviewed, final accepted version for American Mineralogist, published by the Mineralogical Society of America.
The published version is subject to change. Cite as Authors (Year) Title. American Mineralogist, in press.
DOI: https://doi.org/10.2138/am-2022-8552. http://www.minsocam.org/

859 Keith M, Smith DJ, Doyle K, Holwell DA, Jenkin GRT, Barry TL, Becker J and Rampe J
860 (2020) Pyrite chemistry: A new window into Au-Te ore-forming processes in alkaline
861 epithermal districts, Cripple Creek, Colorado. Geochimica et Cosmochimica Acta
862 274: 172-191.
863 Kelley KD and Spry PG (2016) Critical Elements in Alkaline Igneous Rock-Related
864 Epithermal Gold Deposits, in Verplanck PL, and Hitzman MW (Eds.), Rare Earth
865 and Critical Elements in Ore Deposits. Society of Economic Geologists Inc., pp
866 195-216.
867 Kelley KD, Romberger SB, Beaty DW, Pontius JA, Snee LW, Stein HJ and Thompson
868 TB (1998) Geochemical and geochronological constraints on the genesis of Au-Te
869 deposits at Cripple Creek, Colorado. Economic Geology 93: 981-1012.
870 Kennedy BM and van Soest MC (2007) Flow of Mantle Fluids Through the Ductile
871 Lower Crust: Helium Isotope Trends. Science 318: 1433-1436.
872 Kim KH, Lee S, Nagao K, Sumino H, Yang K and Lee JI (2012) He-Ar-H-O isotopic
873 signatures in Au-Ag bearing ore fluids of the Sunshin epithermal gold-silver ore
874 deposits, South Korea. Chemical Geology 320: 128-39.
875 Landis GP and Hofstra AH (2012) Ore genesis constraints on the Idaho cobalt belt from
876 fluid inclusion gas, noble gas isotope, and ion ratio analyses. Economic Geology 107:
877 1189-1205.

Always consult and cite the final, published document. See http:/www.minsocam.org or GeoscienceWorld

This is the peer-reviewed, final accepted version for American Mineralogist, published by the Mineralogical Society of America.
The published version is subject to change. Cite as Authors (Year) Title. American Mineralogist, in press.
DOI: https://doi.org/10.2138/am-2022-8552. http://www.minsocam.org/

878 Landis GP and Rye RO (2005) Characterization of gas chemistry and noble-gas isotope
879 ratios of inclusion fluids in magmatic-hydrothermal and magmatic-steam alunite.
880 Chemical Geology 215: 155-184.
881 Li CL (2018) Gold metallogeny and prospecting in the Nenjiang-Heihe tectonic mélange
882 zone, Heilongjiang Province. PhD thesis, China University of Geosciences (Beijing),
883 pp 1-182 (in Chinese with English abstract).
884 Li JY (2006) Permian geodynamic setting of Northeast China and adjacent regions:
885 closure of the Paleo-Asian Ocean and subduction of the Paleo-Pacific Plate. Journal
886 of Asian Earth Sciences 26: 207-224.
887 Li Z, Qin K, Li G, Ishihara S, Jin L, Song G and Meng Z (2014) Formation of the giant
888 Chalukou porphyry Mo deposit in northern Great Xing'an Range, NE China: partial
889 melting of the juvenile lower crust in intra-plate extensional environment. Lithos
890 202-203: 138-156.
891 Li Z, Qin K, Li G, Jin L, Song G and Han R (2019) Incursion of meteoric water triggers
892 molybdenite precipitation in porphyry Mo deposits: A case study of the Chalukou
893 giant Mo deposit. Ore Geology Reviews 109: 144-162.
894 Liu JL, Bai XD, Zhao SJ, Tran MD, Zhang ZC, Zhao ZD, Zhao HB and Lu J (2011)
895 Geology of the Sandaowanzi telluride gold deposit of the northern Great Xing'an
896 Range, NE China: Geochronology and tectonic controls. Journal of Asian Earth
897 Sciences 41: 107-118.
898 Liu JL, Zhao SJ, Cook NJ, Bai XD, Zhang ZC, Zhao ZD and Lu J (2013) Bonanza-grade

Always consult and cite the final, published document. See http:/www.minsocam.org or GeoscienceWorld

This is the peer-reviewed, final accepted version for American Mineralogist, published by the Mineralogical Society of America.
The published version is subject to change. Cite as Authors (Year) Title. American Mineralogist, in press.
DOI: https://doi.org/10.2138/am-2022-8552. http://www.minsocam.org/

899 accumulations of gold tellurides in the Early Cretaceous Sandaowanzi deposit,
900 northeast China. Ore Geology Reviews 54: 110-126.
901 Liu Y, Sun J, Han J, Ren L, Gu A, Zhao K and Wang C (2019) Origin and evolution of
902 ore-forming fluid for the Gaosongshan gold deposit, Lesser Xing'an Range: Evidence
903 from fluid inclusions, H-O-S-Pb isotopes. Geoscience Frontiers 10: 1961-1980.
904 Lode S, Piercey SJ, Layne GD, Piercey G and Cloutier J (2017) Multiple sulphur and
905 lead sources recorded in hydrothermal exhalites associated with the Lemarchant
906 volcanogenic massive sulphide deposit, central Newfoundland, Canada. Mineralium
907 Deposita 52: 105-128.
908 Lorand JP and Luguet A (2016) Chalcophile and siderophile elements in mantle rocks:
909 Trace elements controlled by trace minerals, in Harvey J and Day JMD (Eds.)
910 Reviews in Mineralogy and Geochemistry, Highly Siderophile and Strongly
911 Chalcophile Elements in High-Temperature Geochemistry and Cosmochemistry, vol.
912 81. Mineralogical Society of America, Washington, D.C., pp 441-488.
913 Lorand JP and Alard O (2010) Determination of selenium and tellurium concentrations in
914 Pyrenean peridotites (Ariege, France): new insight into S/Se/Te systematics of the
915 upper in mantle samples. Chemical Geology 278: 120-130.
916 Manning AH and Hofstra AH (2017) Noble gas data from Goldfield and Tonopah
917 epithermal Au-Ag deposits, ancestral Cascades Arc, USA: Evidence for a primitive
918 mantle volatile source. Ore Geology Reviews 89: 683-700.
919 Mao J, Li Y, Goldfarb R, He Y and Zaw K (2003) Fluid inclusion and noble gas studies

Always consult and cite the final, published document. See http:/www.minsocam.org or GeoscienceWorld

This is the peer-reviewed, final accepted version for American Mineralogist, published by the Mineralogical Society of America.
The published version is subject to change. Cite as Authors (Year) Title. American Mineralogist, in press.
DOI: https://doi.org/10.2138/am-2022-8552. http://www.minsocam.org/

of the Dongping gold deposit, Hebei Province, China: a mantle connection for mineralization? Economic Geology 98: 517-534.

Miao LC, Fan WM, Zhang FQ, Liu DY, Jian P, Shi GH, Tao H and Shi YR (2004) Zircon SHRIMP geochronology of the Xinkailing-Kele complex in the northwestern Lesser Xing'an Range, and its geological implications. Chinese Science Bulletin 49: 201-209.

Miao LC, Liu DY, Zhang FQ, Fan WM, Shi YR and Xie HQ (2007) Zircon SHRIMP U-Pb ages of the "Xinghuadukou Group" in Hanjiayuanzi and Xinlin areas and the "Zhalantun Group" in Inner Mongolia, Da Hinggan Mountains. Chinese Science Bulletin 52: 1112-1124.

Miao LC, Zhang FQ, Zhu MS and Liu DY (2015) Zircon SHRIMP U-Pb dating of metamorphic complexes in the conjunction of the Greater and Lesser Xing'an ranges, NE China: Timing of formation and metamorphism and tectonic implications. Journal of Asian Earth Sciences 114: 634-648.

O'Neil JR and Silberman ML (1974) Stable isotope relations in epithermal Au-Ag deposits. Economic Geology 69: 902-909.

Ozima M and Podosek FA (2002) Noble gas geochemistry, 2nd ed. Cambridge, Cambridge University Press, pp 1-281.

Patten C, Barnes SJ, Mathez EA and Jenner FE (2013) Partition coefficients of chalcophile elements between sulfide and silicate melts and the early crystallization history of sulfide liquid: LA-ICP-MS analysis of MORB sulfide droplets. Chemical

Always consult and cite the final, published document. See http:/www.minsocam.org or GeoscienceWorld

This is the peer-reviewed, final accepted version for American Mineralogist, published by the Mineralogical Society of America.
The published version is subject to change. Cite as Authors (Year) Title. American Mineralogist, in press.
DOI: https://doi.org/10.2138/am-2022-8552. http://www.minsocam.org/

941 Geology 358: 170-188.

942 Pei FP, Xu WL, Yang DB, Zhao QG, Liu XM and Hu ZC (2007) Zircon U-Pb
943 geochronology of basement metamorphic rocks in the Songliao Basin. Chinese
944 Science Bulletin 52: 942-948.

945 Piercey SJ and Kamber BS (2019) Lead isotope geochemistry of shales from the
946 Wolverine volcanogenic massive sulfide deposit, Yukon: Implications for Pb isotope
947 vectoring in exhalative ore systems. Economic Geology 114: 47-66.

948 Qu GS (2008) Lithostratigraphy of Heilongjiang province, China: Wuhan, China
949 University of Geosciences Press, pp 1-301 (in Chinese).

950 Richards JP and Noble SR (1998) Application of radiogenic isotope systems to the timing
951 and origin of hydrothermal processes, in Richards JP and Larson PB (Eds.),
952 Techniques in Hydrothermal Ore Deposits Geology. Society of Economic Geologists
953 Inc., pp 195-233.

954 Richards JP, McCulloch MT, Chappell BW and Kerrich, R (1991) Sources of metals in
955 the Porgera gold deposit, Papua New Guinea: Evidence from alteration, isotope, and
956 noble metal geochemistry. Geochimica et Cosmochimica Acta 55: 565-580.

957 Saunders JA and Brueseke ME (2012) Volatility of Se and Te during subduction-related
958 distillation and the geochemistry of epithermal ores of the western United States.
959 Economic Geology 107: 165-172.

960 Saunders JA, Unger DL, Kamenov GD, Fayek M, Hames WE and Utterback WC (2008)
961 Genesis of Middle Miocene Yellowstone hotspot-related bonanza epithermal Au–Ag

Always consult and cite the final, published document. See http:/www.minsocam.org or GeoscienceWorld

This is the peer-reviewed, final accepted version for American Mineralogist, published by the Mineralogical Society of America.
The published version is subject to change. Cite as Authors (Year) Title. American Mineralogist, in press.
DOI: https://doi.org/10.2138/am-2022-8552. http://www.minsocam.org/

deposits, Northern Great Basin, USA. Mineralium Deposita 43: 715-734.

Sengör AMC, Natal'in BA and Burtman VS (1993) Evolution of the Altaid tectonic collage and Paleozoic crustal growth in Eurasia. Nature 364: 299-307.

Shen JF, Santosh M, Li SR, Li CP, Zhang JQ, Zhang SQ, Alam M, Wang YH and Xu KX (2020) He-Ar, S, Pb and O isotope geochemistry of the Dabaiyang gold deposit: Implications for the relationship between gold metallogeny and destruction of the North China Craton. Ore Geology Reviews 116: 103229.

Shikazono N, Nakata M and Shimizu M (1990) Geochemical, mineralogic and geologic characteristics of Se-and Te-bearing epithermal gold deposits in Japan. Mining Geology 40: 337-352.

Shu P, Ding RX, Ji XY and Qu YM (2007) SHRIMP zircon geochronology of reservoir volcanic rocks in the Qingshen gas field, Songliao Basin. Acta Petrologica et Mineralogica 26: 239-246 (in Chinese with English abstract).

Simmons SF (1995) Magmatic contributions to low-sulfidation epithermal deposits, in Magmas, fluids and ore deposits: Mineralogical Association of Canada Short Course Series 23: 455-477.

Simmons SF, Brown KL and Tutolo BM (2016) Hydrothermal transport of Ag, Au, Cu, Pb, Te, Zn, and other metals and metalloids in New Zealand geothermal systems: Spatial patterns, fluid-mineral equilibria, and implications for epithermal mineralization. Economic Geology 111: 589-618.

Simmons SF, Sawkins FJ and Schlutter DJ (1987) Mantle-derived helium in two

Always consult and cite the final, published document. See http:/www.minsocam.org or GeoscienceWorld

This is the peer-reviewed, final accepted version for American Mineralogist, published by the Mineralogical Society of America.
The published version is subject to change. Cite as Authors (Year) Title. American Mineralogist, in press.
DOI: https://doi.org/10.2138/am-2022-8552. http://www.minsocam.org/

983 Peruvian hydrothermal ore deposits. Nature 329: 429-432.

984 Simmons SF, White NC and John DA (2005) Geological characteristics of epithermal
985 precious and base metal deposits, in Hedenquist JW, Thompson JFH, Goldfarb RJ,
986 and Richards JP (Eds.), One Hundredth Anniversary Volume. Society of Economic
987 Geologists Inc., pp 485-522.

988 Song G, Cook NJ, Wang L, Qin K, Ciobanu CL and Li G (2019) Gold behavior in
989 intermediate sulfidation epithermal systems: A case study from the Zhengguang gold
990 deposit, Heilongjiang Province, NE-China. Ore Geology Reviews 106: 446-462.

991 Spry PG, Chryssoulis S and Ryan CG (2004) Process mineralogy of gold: Gold from
992 telluride-bearing ores. JOM 56: 60-62.

993 Stacey JS and Kramers JD (1975) Approximation of terrestrial lead isotope evolution by
994 a two-stage model. Earth and Planetary Science Letters 26: 207-221.

995 Sui ZM, Ge WC, Wu FY, Zhang JH, Xu XC and Cheng RY (2007) Zircon U-Pb ages,
996 geochemistry and its petrogenesis of Jurassic granites in northeastern part of the Da
997 Hinggan Mts. Acta Petrologica Sinica 23: 461-480 (in Chinese with English
998 abstract).

999 Sun JG, Zhang Y, Han SJ, Men LJ, Li YX, Chai P and Yang F (2013) Timing of
1000 formation and geological setting of low-sulphidation epithermal gold deposits in the
1001 continental margin of NE China. International Geology Review 55: 608-632.

1002 Tan J, Wei J, He H, Su F, Li Y, Fu L, Zhao S, Xiao G, Zhang F, Xu J and Liu Y (2018)
1003 Noble gases in pyrites from the Guocheng-Liaoshang gold belt in the Jiaodong

Always consult and cite the final, published document. See http:/www.minsocam.org or GeoscienceWorld

This is the peer-reviewed, final accepted version for American Mineralogist, published by the Mineralogical Society of America.
The published version is subject to change. Cite as Authors (Year) Title. American Mineralogist, in press.
DOI: https://doi.org/10.2138/am-2022-8552. http://www.minsocam.org/

province: Evidence for a mantle source of gold. Chemical Geology 480: 105-115.

Tatsumoto M, Knight RJ and Allegre CJ (1973) Time differences in the formation of meteorites as determined from the ratio of lead-207 to lead-206. Science 180: 1279-1283.

Tosdal RM, Cline JS, Fanning CM and Wooden JL (2003) Lead in the Getchell-Turquoise Ridge Carlin-type gold deposits from the perspective of potential igneous and sedimentary rock sources in northern Nevada: Implications for fluid and metal sources. Economic Geology 98: 1189-1211.

Tosdal RM, Wooden JL and Bouse RM (1999) Pb isotopes, ore deposits, and metallogenetic terranes, in Lambert DD and Ruiz J (Eds.), Application of Radiogenic Isotopes to Ore Deposit Research and Exploration. Society of Economic Geologists Inc., pp 1-28.

Wang L, Percival JB, Hedenquist JW, Hattori K and Qin K (2021) Alteration mineralogy of the Zhengguang epithermal Au-Zn deposit, Northeast China: Interpretation of shortwave infrared analyses during mineral exploration and assessment. Economic Geology 116: 389-406.

Wang PJ, Liu ZJ, Wang SX and Song WH (2002) $^{40}Ar/^{39}Ar$ and K/Ar dating of the volcanic rocks in the Songliao basin, NE China: Constraints on stratigraphy and basin dynamics. International Journal of Earth Sciences 91: 331-340.

Wang Y, Zeng Q, Zhou L, Chu S, and Guo Y (2016) The sources of ore-forming material in the low-sulfidation epithermal Wulaga gold deposit, NE China: Constraints from S,

Always consult and cite the final, published document. See http:/www.minsocam.org or GeoscienceWorld

This is the peer-reviewed, final accepted version for American Mineralogist, published by the Mineralogical Society of America.
The published version is subject to change. Cite as Authors (Year) Title. American Mineralogist, in press.
DOI: https://doi.org/10.2138/am-2022-8552. http://www.minsocam.org/

1025 Pb isotopes and REE pattern. Ore Geology Reviews 76: 140-151

1026 Wang Y, Zhang FQ, Zhang DW, Miao LC, Li TS, Xie HQ, Meng QR and Liu DY (2006)
1027 Zircon SHRIMP U-Pb dating of meta-diorite from the basement of the Songliao
1028 Basin and its geological significance. Chinese Science Bulletin 51: 1877-1883.

1029 Wang YB, Liu JM, Sun SK, Li Y, Li FY and Hu HT (2012) Zircon U-Pb geochronology,
1030 petrogenesis and geological implication of ore-bearing granodiorite porphyry in the
1031 Wulaga gold deposit, Heilongjiang Province. Acta Petrologica Sinica 28: 557-570.

1032 White NC, Zhang D, Hong H, Liu L, Sun W and Zhang M (2019) Epithermal Gold
1033 Deposits of China-An Overview, in Chang Z and Goldfarb RJ (Eds.), Mineral
1034 Deposits of China. Society of Economic Geologists Inc., pp 235-262.

1035 Wilde SA Dorsett-Bain HL and Liu JL (1997) The identification of a Late Pan-African
1036 granulite facies event in Northeastern China: SHRIMP U-Pb zircon dating of the
1037 Mashan Group at Liu Mao, Heilongjiang Province, China Proceedings of the 30th
1038 IGC: Precambrian Geology and Metamorphic Petrology, VSP International, Science
1039 Publishers, Amsterdam, 17, pp 59-74.

1040 Wilde SA, Wu FY and Zhang XZ (2003) Late Pan-African magmatism in Northeastern
1041 China: SHRIMP U-Pb zircon evidence for igneous ages from the Mashan Complex.
1042 Precambrian Research 122: 311-327.

1043 Wilde SA, Zhang XZ and Wu FY (2000) Extension of a newly-identified 500 Ma
1044 metamorphic terrain in Northeast China: Further U-Pb SHRIMP dating of the
1045 Mashan Complex, Heilongjiang Province, China. Tectonophysics 328: 115-130.

Always consult and cite the final, published document. See http:/www.minsocam.org or GeoscienceWorld

This is the peer-reviewed, final accepted version for American Mineralogist, published by the Mineralogical Society of America.
The published version is subject to change. Cite as Authors (Year) Title. American Mineralogist, in press.
DOI: https://doi.org/10.2138/am-2022-8552. http://www.minsocam.org/

1046 Woodhead J (2002) A simple method for obtaining highly accurate Pb isotope data by
1047 MC-ICP-MS. Journal of Analytical Atomic Spectrometry 17: 1381-1385.
1048 Wu FY, Sun DY, Li HM and Wang XL (2000) Zircon U-Pb ages of the basement rocks
1049 beneath the Songliao Basin, NE China. Chinese Science Bulletin 45: 1514-1518.
1050 Wu FY, Yang JH, Lo CH, Wilde SA, Sun DY and Jahn BM (2007) The Heilongjiang
1051 Group: A Jurassic accretionary complex in the Jiamusi Massif at the western Pacific
1052 margin of northeastern China. Island Arc 16: 156-172.
1053 Xu WL, Pei FP, Gao FH, Yang DB and Bu YJ (2008) Zircon U-Pb age from basement
1054 granites in Yishu graben and its tectonic implications. Earth Science-Journal of China
1055 University of Geosciences 33: 145-150 (in Chinese with English abstract).
1056 Yu YX, Xu H, Wu XK, Yang LJ, Tian Z, Gao S and Wang QS (2012) Characteristics of
1057 the Au-Ag-Te minerals and its ore-forming fluids in Sandaowanzi gold deposit,
1058 Heilongjiang Province. Acta Petrologica Sinica 28: 345-356 (in Chinese with English
1059 abstract).
1060 Zhai DG, Liu JJ, Edward MR and Wang JP (2015) Geochronological and He-Ar-S
1061 isotopic constraints on the origin of the Sandaowanzi gold-telluride deposit,
1062 northeastern China. Lithos 212: 338-352.
1063 Zhai DG, Williams-Jones AE, Liu JJ, Tombros SF and Cook NJ (2018) Mineralogical,
1064 fluid inclusion and multiple isotope (H-O-S-Pb) constraints on the genesis of the
1065 Sandaowanzi epithermal Au-Ag-Te deposit, NE China. Economic Geology 113:
1066 1359-1382.

Always consult and cite the final, published document. See http:/www.minsocam.org or GeoscienceWorld

This is the peer-reviewed, final accepted version for American Mineralogist, published by the Mineralogical Society of America.
The published version is subject to change. Cite as Authors (Year) Title. American Mineralogist, in press.
DOI: https://doi.org/10.2138/am-2022-8552. http://www.minsocam.org/

1067 Zhang C, Wang E, Bi Z, Han R, Shao J, Liu B, Chen J and Zeng N (2019)
1068 Geochronology and isotope geochemistry studies of an epithermal gold deposit in the
1069 northern Lesser Khingan Range, NE China: The Gaosongshan example. Ore Geology
1070 Reviews 105: 356-374.
1071 Zhang FQ, Pang YM, Yang SF, Dong CW, Chen HL and Shu P (2007) Geochronology of
1072 zircon SHRIMP, geochemistry and its implication of the volcanic rocks from
1073 Yingcheng Formation in depression area, north of Songliao Basin. Acta Geologica
1074 Sinica 81: 1249-1259 (in Chinese with English abstract).
1075 Zhang JH, Ge WC, Wu FY, Wilde SA, Yang JH and Liu XM (2008) Large-scale Early
1076 Cretaceous volcanic events in the northern Great Xing'an Range, northeastern China.
1077 Lithos 102: 138-157.
1078 Zhang Z and Mao J (1995) Geology and geochemistry of the Dongping gold telluride
1079 deposit, Heibei province, north China. International Geology Review 37:
1080 1094-1108.
1081 Zhang Z, Mao J, Wang Y, Pirajno F, Liu J and Zhao Z (2010) Geochemistry and
1082 geochronology of the volcanic rocks associated with the Dong'an adularia–sericite
1083 epithermal gold deposit, Lesser Hinggan Range, Heilongjiang province, NE China:
1084 Constraints on the metallogenesis. Ore Geology Reviews 37: 158-174.
1085 Zhao YD, Che JY, Li SC, Wang KL, Zhao J, Wu DT, Xu FM and Sun QS (2015) Late
1086 Jurassic rapakivi granite and its geological implication of the northeast Great
1087 Xing'an Range, China: Chinese Mineral Geochemistry Society 15th Annual

Always consult and cite the final, published document. See http:/www.minsocam.org or GeoscienceWorld

This is the peer-reviewed, final accepted version for American Mineralogist, published by the Mineralogical Society of America.
The published version is subject to change. Cite as Authors (Year) Title. American Mineralogist, in press.
DOI: https://doi.org/10.2138/am-2022-8552. http://www.minsocam.org/

Conference Abstract Book, v 1 (in Chinese).

Zhao ZH, Sun JG, Li GH, Xu WX, Lv CL, Wu S, Guo Y, Liu J and Ren L (2019b) Early Cretaceous gold mineralization in the Lesser Xing'an Range of NE China: the Yongxin example. International Geology Review 61: 1522-1549.

Zhao ZH, Sun JG, Li GH, Xu WX, Lv CL, Wu S, Guo Y, Ren L and Hu ZX (2019a) Age of the Yongxin Au deposit in the Lesser Xing'an Range: Implications for an Early Cretaceous geodynamic setting for gold mineralization in NE China. Geological Journal 54: 2525-2544.

Zhi Y (2015) Study on the mineralization tectonic setting and genesis of the Dong'an gold deposit, Lesser Khingan Range. MSc thesis, Jilin University, Changchun, China, pp 1-82 (in Chinese with English abstract).

Zhi Y, Li B, Xi A, Xu Q, Zhang L, Sun Y, Chang J and Peng B (2016) Geochronology and geochemistry of the major host rock of the Dong'an gold deposit, Lesser Khingan Range: implications for petrogenesis and metallogenic setting during the Early–Middle Jurassic in northeast China. Geochemistry 76: 257-74.

Zhou JB, Wilde SA, Zhang XZ, Zhao GC, Zheng CQ, Wang YJ and Zhang XH (2009) The onset of Pacific margin accretion in NE China: evidence from the Heilongjiang high-pressure metamorphic belt. Tectonophysics 478: 230-246.

Figure captions

Always consult and cite the final, published document. See http:/www.minsocam.org or GeoscienceWorld

Fig. 1. (a) Regional geologic map showing the location of Te-bearing epithermal Au-Ag deposits in north Heilongjiang province, NE China (after Gao 2017; Zhao et al. 2019a, b; Gao et al., 2022). The inset shows the location of the regional map relative to crustal blocks in NE China. Numbers are $^{206}Pb/^{204}Pb$ values from host rocks by bulk analysis (Appendix B, Table B2). (b) Stratigraphic section of north Heilongjiang province, showing Cretaceous intrusive rock and host rocks for the deposits.

Abbreviation: O = Ordovician, S = Silurian, D = Devonian, C = Carboniferous, P = Permian, T = Triassic, J = Jurassic, K = Cretaceous, N = Neogene, Q = Quaternary, LS = low sulfidation, IS = intermediate sulfidation.

Fig. 2. Geologic maps and cross sections of (a) Sandaowanzi (after Liu et al. 2013; Gao et al. 2017a; 2022), (b) Yongxin (after Zhao et al. 2019a, b), (c) Dong'an (after Zhang et al. 2010), and (d) Tuanjiegou (after Wang et al. 2012) deposits.

Fig. 3. Photographs showing mineralogy and textures representative of ores from Sandaowanzi (a–d), Yongxin (e–g), Dong'an (h–k), and Tuanjiegou (l–o) Te-bearing epithermal Au-Ag deposits (Gao et al., 2022). (a) and (b) Au-Ag tellurides and chalcopyrite in colloform quartz vein. (c) Au-Ag tellurides and chalcopyrite with crystalline quartz vug. (d) Crystalline quartz and laumontite. (e) Quartz, sericite and pyrite alteration. (f) Brecciated quartz vein. (g) Quartz, sericite and calcite alteration. (h) Quartz and adularia vein hosted in andesite. (i) Quartz, adularia and chlorite in colloform

Always consult and cite the final, published document. See http:/www.minsocam.org or GeoscienceWorld

vein. (j) Bladed quartz. (k) Late-stage fluorite and quartz vein hosted in granite. (l) Marcasite and quartz vein hosted in granodiorite. (m) Au-Ag telluride and sulfide vein. (n) Stibnite and quartz vein. (o) Colloform calcite vein.

Fig. 4. Pre laser ablation images of telluride and sulfide minerals analyzed for Pb isotope compositions using the femtosecond (*fs)* laser ablation multicollector inductively coupled plasma mass spectrometry (*fs* LA-MC-ICP-MS). Tracks from Sandaowanzi (a–e), Yongxin (f), Dong'an (g–h), and Tuanjiegou (i). Figure 4f is a reflected images others are secondary electron images. (a) Stützite coexisting with hessite in colloform quartz vein. (b) Sylvanite coexisting with petzite in colloform quartz vein. (c) Calaverite coexisting with petzite in colloform quartz vein. (d) Altaite coexisting with petzite, sylvanite and hessite in colloform quartz vein. (e) Pyrite in andesite breccia replaced by quartz. (f) Altaite coexisting with galena and sphalerite in colloform quartz and adularia vein. (g) Galena replacing pyrite in quartz vein. (h) Argentite coexisting with galena, sphalerite and replacing pyrite in colloform quartz and adularia vein. (i) Pyrite associated with native gold in quartz vein. The ellipses mark areas that were subsequently ablated.
Abbreviation: Alt = altaite, Arg = argentite, Cav = calaverite, Cp = chalcopyrite, Gn = galena, Hes = hessite, Ptz = petzite, Py = pyrite, Qz = quartz, Sp = sphalerite, Stü = stützite, Syl = sylvanite.

Fig. 5. Photomicrographs showing the textures of gangue minerals and fluid inclusions

Always consult and cite the final, published document. See http:/www.minsocam.org or GeoscienceWorld

from Sandaowanzi (a–c), Yongxin (d–f), Dong'an (g–i) and Tuanjiegou (j–l). (a) Abundant liquid rich fluid inclusions in quartz crystals in colloform vein. (b) Fine-grained quartz with a colloform texture. (c) Abundant liquid rich fluid inclusions in quartz crystals in late-stage quartz vein. (d) Quartz associated with tellurides. (e) Late-stage crystalline quartz. (f) Calcite coexisting with quartz. (g) Early stage bladed quartz and recrystallized quartz. (h) Quartz and adularia in colloform vein. (i) Late-stage fluorite vein. (j) Quartz and pyrite vein. (k) Abundant liquid rich fluid inclusions in quartz crystals. (l) Calcite crystals in colloform vein.

Abbreviation: Adl = adularia, Cal = calcite, Flr = fluorite, Py = pyrite, Qz = quartz, FIs = fluid inclusions, FQ = fine-grained quartz.

Fig. 6. Photomicrographs of fluid inclusions in quartz, fluorite, and calcite from Sandaowanzi (a–c), Yongxin (d–g), Dong'an (g–l), and Tuanjiegou (m–o). Yongxin has CO_2-bearing fluid inclusions (Fig. 5f, g). Others are L-V type in the H_2O-NaCl system.

Abbreviation: Cal = calcite, Flr = fluorite, Qz = quartz.

Fig. 7. Lead isotope compositions of telluride, sulfide and gangue minerals determined by femtosecond (*fs*) laser ablation multicollector inductively coupled plasma mass spectrometry (*fs* LA-MC-ICP-MS) from Sandaowanzi, Dong'an, Yongxin, and Tuanjiegou. (a) $^{207}Pb/^{204}Pb$ versus $^{206}Pb/^{204}Pb$. (b) $^{208}Pb/^{204}Pb$ versus $^{206}Pb/^{204}Pb$. (c) and (d) Enlarged areas from (a) and (b), respectively. Lead isotopes of Early Cretaceous

Always consult and cite the final, published document. See http:/www.minsocam.org or GeoscienceWorld

igneous rocks and pyrite in the area are from Wang et al. (2012), Han (2013), Gao et al. (2017a), Li (2018), Zhang et al. (2019). (e) $^{206}Pb/^{207}Pb$ versus $^{208}Pb/^{207}Pb$ (f). $^{207}Pb/^{206}Pb$ versus $^{208}Pb/^{206}Pb$. Country rock trends in Fig. 7e are based on Early Cretaceous rock plots (see Appendix A Fig. A1). Rock contaminated trends in Fig. 7f are from regional rocks in NE China (see Appendix A Fig. A1). Sulfide data points in Fig. 7a, b are based on Early Cretaceous sulfide plots (see Appendix A Fig. A2).

Fig. 8. Lead isotope evolution model for lead sources in epithermal Au-Ag deposits (Northern Heilongjiang province, NE China). Colors of characters, numbers and lines: Sandaowanzi = red, Yongxin = yellow, Dong'an = green, and Tuanjiegou = blue. The model age of both lead sources is based on the maximum and minimum ages for each deposit. Values of $\mu1_{max}$ and $\mu1_{min}$ are calculated values from lead evolution models. $\mu1$ corresponds to the $^{238}U/^{204}Pb$ ratio of mantle (7.192; Tatsumoto et al., 1973), and lead source; $t1_{max}$ and $t1_{min}$ correspond to the age of crust formation for lead sources 1 and 2 in each deposit, respectively.

Fig. 9. Noble gas plots of fluid inclusion extracts showing early, main, and late-stage minerals. (a) Molar He abundance versus R/R_A. (b) Molar $CO_2/^3He$ versus R/R_A plot (dashed vertical lines; Ozima and Podosek 2002). (c) Molar $^{36}Ar/^4He$ versus R/R_A diagram with binary mixing lines between air/air-saturated water (ASW), mantle, and crust. (d) Molar $^{20}Ne/^4He$ versus R/R_A diagram with binary mixing lines between

Always consult and cite the final, published document. See http:/www.minsocam.org or GeoscienceWorld

1193 air/air-saturated water (ASW), mantle, and crust. (e) Molar $^{20}Ne/^{22}Ne$ versus R/R_A plot of
1194 fluid inclusion extracts relative to those of air, crust and mantle sources (dashed lines).
1195 Published data of Sandaowanzi and Yongxin deposits are from Yu et al. (2012), Zhai et al.
1196 (2015), and Li (2018). Geothermal data from the Cascades arc and Basin and Range
1197 (B&R) province are from Kennedy and van Soest (2007). The R/R_A ratios of air, mantle,
1198 and crustal are from Graham (2002) and Hilton et al. (2002). Vertical dashed line shows
1199 typical pattern of increasing mantle ^3He with decreasing abundance of radiogenic ^4He
1200 (Landis and Rye 2005; Landis and Hofstra 2012; Hofstra et al. 2016; Manning and
1201 Hofstra 2017). Bold dashed line shows epithermal and deeper intrusion-related systems.
1202 Shadow and line circles are different areas.
1203
1204 Fig. 10. Homogenization temperatures and salinities of fluid inclusions from the
1205 Sandaowanzi, Yongxin, Dong'an, and Tuanjiegou deposits in the North Heilongjiang Belt,
1206 NE China. Representative samples overlay with R/R_A from the same sample. Symbol
1207 shape with color line is for data points from each deposit. Color filling is the stage. Shape
1208 size is R/R_A value. Grey field and colored lines encompass data from different deposits
1209 and are determined by 2D density contours. Secondary fluid inclusions (FIs) are formed
1210 when fluids are trapped after the crystal growth is complete.
1211
1212 Fig. 11. Schematic models for fluid source and evolution in epithermal Au-Ag deposits in
1213 north Heilongjiang province, NE China. μ1 corresponds to the $^{238}U/^{204}Pb$ ratio of mantle

Always consult and cite the final, published document. See http:/www.minsocam.org or GeoscienceWorld

This is the peer-reviewed, final accepted version for American Mineralogist, published by the Mineralogical Society of America.
The published version is subject to change. Cite as Authors (Year) Title. American Mineralogist, in press.
DOI: https://doi.org/10.2138/am-2022-8552. http://www.minsocam.org/

(7.192; Tatsumoto et al., 1973), and Pb source. He_{mantle} is referring to typical pattern of increasing mantle ^{3}He with decreasing abundance of radiogenic ^{4}He (Landis and Rye 2005; Landis and Hofstra 2012; Hofstra et al. 2016; Manning and Hofstra 2017). Colors of characters and numbers in models: Sandaowanzi = red, Yongxin = yellow, Dong'an = green, and Tuanjiegou = blue.

List of tables

Table 1. Characteristics of Early Cretaceous adularia-sericite epithermal Au-Ag deposits in the North Heilongjiang Belt, NE China.

Table 2. Minerals analyzed from Sandaowanzi, Yongxin, Dong'an, and Tuanjiegou deposits in the North Heilongjiang Belt, NE China.

Table 3. In situ Pb isotope results for minerals from Sandaowanzi, Yongxin, Dong'an, and Tuanjiegou in the North Heilongjiang Belt, NE China. "nd" (not determined) was due to insufficient ^{204}Pb signal.

Table 4. Noble gas isotope results of fluid inclusions from Sandaowanzi, Yongxin, Dong'an and Tuanjiegou in the North Heilongjiang Belt, NE China.

Always consult and cite the final, published document. See http:/www.minsocam.org or GeoscienceWorld

This is the peer-reviewed, final accepted version for American Mineralogist, published by the Mineralogical Society of America.
The published version is subject to change. Cite as Authors (Year) Title. American Mineralogist, in press.
DOI: https://doi.org/10.2138/am-2022-8552. http://www.minsocam.org/

Table 5. Homogenization temperatures and salinities of fluid inclusions from Sandaowanzi, Yongxin, Dong'an and Tuanjiegou in the North Heilongjiang Belt, NE China.

Table 6. Summary of lead and noble gas isotopes, fluid inclusion microthermometry, and the main features of Te-rich and Te-poor deposits in the North Heilongjiang Belt, NE China.

Appendix

Appendix A: Lead isotope framework of northern Heilongjiang province and descriptions of the Au-Ag deposits.

Appendix B: Fluid inclusion, Pb isotope, and noble gas isotope data.

Table B1. Detailed homogenization temperature and salinity of fluid inclusions from Sandaowanzi, Yongxin, Dong'an, and Tuanjiegou in the North Heilongjiang Belt, NE China.

Table B2. Published Pb isotope data from igneous rocks, metamorphic rocks, and sulfide minerals in the North Heilongjiang Belt, NE China.

Always consult and cite the final, published document. See http:/www.minsocam.org or GeoscienceWorld

This is the peer-reviewed, final accepted version for American Mineralogist, published by the Mineralogical Society of America.
The published version is subject to change. Cite as Authors (Year) Title. American Mineralogist, in press.
DOI: https://doi.org/10.2138/am-2022-8552. http://www.minsocam.org/

1256

1257 Table B3. Published noble gas isotope data from epithermal and intrusion-related Au

1258 deposits in China and South Korea.

1259

Always consult and cite the final, published document. See http:/www.minsocam.org or GeoscienceWorld

This is the peer-reviewed, final accepted version for American Mineralogist, published by the Mineralogical Society of America.
The published version is subject to change. Cite as Authors (Year) Title. American Mineralogist, in press.
DOI: https://doi.org/10.2138/am-2022-8552. http://www.minsocam.org/

1 Table 1. Characteristics of Early Cretaceous adularia-sericite epithermal Au-Ag deposits in the North Heilongjiang Belt, NE China.

Deposit	**Sandaowanzi**	**Yongxin**	**Dong'an**	**Tuanjiegou**
Type	Te-rich	Te-rich	Te-poor	Te-poor
Tectonic location	Xing'an Block	Xing'an Block	Songliao Block	Jiamusi Massif
Production	22t Au at a grade of 13.98 g/t	20t Au at a grade of 4.1 g/t	24t Au at a grade of 8.8 g/t	80t Au at a grade of 4.0 g/t
Alteration	Quartz, pyrite, sericite, calcite, chlorite, and epidote	Quartz, pyrite, sericite, carbonates, anhydrite, and chlorite	Quartz, pyrite, sericite, calcite, and chlorite	Quartz, pyrite, sericite, calcite, and chlorite
Gangue minerals in the veins	Quartz, chalcedony, calcite, laumontite, anhydrite and zeolite	Quartz, pyrite, and calcite	Quartz, adularia, chalcedony, chlorite, calcite, pyrite and fluorite	Quartz, pyrite, marcasite, and carbonates
Ore minerals in the veins	Abundant Au-Ag-tellurides (>95% in metal minerals), rare chalcopyrite, galena, and sphalerite	Pyrite, chalcopyrite, galena, sphalerite, native gold, Au-Ag-tellurides, and Bi-tellurides	Electrum, native gold, Ag-sulfides, Ag-sulfates, Au-Ag-tellurides (low content), pyrite, chalcopyrite, galena, and sphalerite	Pyrite, marcasite, stibnite, chalcopyrite, galena, sphalerite and native gold
Pb isotopes	Volcanic rocks and pyrite are similar	Volcanic rocks, dikes and pyrite are similar	Pyrite is similar to the regional volcanic rocks	Granodioritic porphyry and pyrite are similar
He-Ar isotopes	Quartz, pyrite, chalcopyrite and tellurides: more crust contaminations of pyrite	Gold-bearing pyrite: more mantle compositions	Quartz, adularia, pyrite and fluorite: more crust contaminations of pyrite	Pyrite, quartz, calcite
Ages	Volcanic rocks, dikes, and hydrothermal pyrite, quartz and sericite are similar in age (~120 Ma)	Volcanic rocks, dikes, and hydrothermal pyrite are similar in age (~114 Ma)	Volcanic rocks, and hydrothermal sericite are similar in age (~108 Ma)	Porphyry, dikes, and hydrothermal pyrite are similar in age (~108 Ma)

Always consult and cite the final, published document. See http:/www.minsocam.org or GeoscienceWorld

This is the peer-reviewed, final accepted version for American Mineralogist, published by the Mineralogical Society of America.
The published version is subject to change. Cite as Authors (Year) Title. American Mineralogist, in press.
DOI: https://doi.org/10.2138/am-2022-8552. http://www.minsocam.org/

Table 2. Minerals analyzed from Sandaowanzi, Yongxin, Dong'an, and Tuanjiegou deposits in the North Heilongjiang Belt, NE China.

Deposit	**Sandaowanzi**		**Dong'an**		**Yongxin**		**Tuanjiegou**	
Isotope systems	Lead	Noble gas	Lead	Noble gas	Lead	Noble gas	Lead	Noble gas
Early stage	Py	Py[1], Qtz		Qz, Py		Qz	Pl	Qz
Main stage	Alt, Hes, Ptz, Syl, Stü, Cp, Sp	Cp[1], Ptz[1], Qtz	Alt, Gn, Arg, Py, Adl, Sp, Fer[2]	Adl	Alt, Gn, Py	Py	Gn, Py	Py
Late stage	Cal			Qz, Fl		Cal	Cal	Cal

[1] Cite from published data, see Appendix B.

Abbreviation: Adl = adularia, Alt = altaite, Arg = argentite, Cal = calcite, Cav = calaverite, Cp = chalcopyrite, Gn = galena, Hes = hessite, Pl = plagioclase, Ptz = petzite, Py = pyrite, Qz = quartz, Sp = sphalerite, Stü = stützite, Syl = sylvanite.

Table 3. In situ Pb isotope results for minerals from Sandaowanzi, Yongxin, Dong'an, and Tuanjiegou in the North Heilongjiang Belt, NE China.

Location	**Mineral**	**Sample and description**	**$^{208}Pb/^{204}Pb$**	**SE**	**$^{207}Pb/^{204}Pb$**	**SE**	**$^{206}Pb/^{204}Pb$**	**SE**	**$^{208}Pb/^{206}Pb$**	**SE**	**$^{207}Pb/^{206}Pb$**	**SE**
Sandaowanzi	Alt	90CM21-1 area 2 altaite line 1	38.152	0.003	15.539	0.003	18.274	0.003	2.0880	0.0004	0.8505	0.0001
	Alt	90CM21-1 area 2 altaite line 2	38.105	0.003	15.525	0.003	18.263	0.003	2.0866	0.0004	0.8503	0.0001
	Sp	90CM21-1 area 2 sphalerite line 1	nd		nd		nd		2.0872	0.0004	0.8499	0.0001
	Ptz	90CM21-1 area 2 petzite line 1	38.138	0.003	15.534	0.003	18.278	0.003	2.0866	0.0004	0.8501	0.0001
	Hes	90CM21-1 area 1 hessite line 1	nd		nd		nd		2.0857	0.0004	0.8501	0.0001
	Cal	90CM21-1 area 1 calcite line 2	nd		nd		nd		2.1082	0.0004	0.8592	0.0001
	Ptz+Hes	90CM21-1 area 1 petzite + hessite line 4	nd		nd		nd		2.0856	0.0004	0.8501	0.0001
	Py	90CM21-1 area 3 pyrite line 1	nd		nd		nd		2.0844	0.0004	0.8492	0.0001
	Syl	130CM23-10 area 1 sylvanite line 2	nd		nd		nd		2.0824	0.0004	0.8486	0.0001
	Alt	130CM23-14-1 area 3 altaite line 1	38.149	0.007	15.534	0.003	18.279	0.003	2.0872	0.0001	0.8501	0.0001
	Alt	130CM23-14-1 area 3 altaite line 1 rerun	38.173	0.007	15.542	0.003	18.285	0.003	2.0878	0.0001	0.8502	0.0001
	Alt	130CM23-14-1 area 3 altaite line 2	38.164	0.007	15.539	0.003	18.283	0.003	2.0875	0.0001	0.8501	0.0001
	Py	130CM23-14-1 area 5 pyrite spot 1	nd		nd		nd		2.0936	0.0001	0.8538	0.0001
	Py	130CM23-14-1 area 5 pyrite spot 2	nd		nd		nd		2.0906	0.0001	0.8534	0.0001
Yongxin	Alt	180-29-232.5 area 3 altaite spot 1	37.976	0.007	15.526	0.003	18.139	0.003	2.0937	0.0001	0.8562	0.0001
	Alt	180-29-232.5 area 3 altaite spot 2	37.962	0.007	15.518	0.003	18.128	0.003	2.0942	0.0001	0.8563	0.0001
	Alt	180-29-232.5 area 3 altaite spot 3	nd		nd		nd		2.0946	0.0001	0.8571	0.0001
	Py	180-29-232.5 area 3 pyrite line 1	nd		nd		nd		2.0936	0.0001	0.8559	0.0001
	Gn	177.5-3-200 area 1 galena spot 1	37.949	0.003	15.509	0.003	18.127	0.003	2.0936	0.0004	0.8558	0.0001
	Gn	177.5-3-200 area 1 galena spot 2	37.949	0.003	15.509	0.003	18.128	0.003	2.0935	0.0004	0.8558	0.0001
	Py	177.5-3-200 area 1 galena line 1	nd		nd		nd		2.0909	0.0004	0.8545	0.0001
	Py	177.5-3-200 area 2 galena line 1	nd		nd		nd		2.0902	0.0004	0.8535	0.0001

This is the peer-reviewed, final accepted version for American Mineralogist, published by the Mineralogical Society of America.
The published version is subject to change. Cite as Authors (Year) Title. American Mineralogist, in press.
DOI: https://doi.org/10.2138/am-2022-8552. http://www.minsocam.org/

Dong'an	Gn	36-6-221.5 area 1 galena spot 1	38.533	0.003	15.603	0.003	18.864	0.003	2.0427	0.0004	0.8273	0.0001
	Gn	36-6-221.5 area 1 galena spot 2	38.500	0.003	15.593	0.003	18.855	0.003	2.0419	0.0004	0.8271	0.0001
	Arg	36-6-221.5 area 1 argentite line 1	38.513	0.003	15.601	0.003	18.865	0.003	2.0416	0.0004	0.8271	0.0001
	Py	36-6-221.5 area 1 pyrite line 1	38.504	0.003	15.596	0.003	18.855	0.003	2.0418	0.0004	0.8273	0.0001
	Sp	36-6-221.5 area 1 sphalerite possibly shot AgS	38.469	0.003	15.583	0.003	18.846	0.003	2.0413	0.0004	0.8271	0.0001
	Gn	36-6-221.5 area 2 galena spot 1	38.512	0.003	15.598	0.003	18.860	0.003	2.0421	0.0004	0.8272	0.0001
	Arg	36-6-221.5 area 2 argentite spot 1	nd		nd		nd		2.0384	0.0004	0.8263	0.0001
	Gn	36-6-221.5 area 3 galena spot 1	38.503	0.003	15.597	0.003	18.852	0.003	2.0424	0.0004	0.8275	0.0001
	Gn	36-6-221.5 area 4 galena spot 1	38.510	0.003	15.599	0.003	18.845	0.003	2.0436	0.0004	0.8280	0.0001
	Gn	36-6-221.5 area 5 galena spot 1	38.540	0.003	15.605	0.003	18.871	0.003	2.0423	0.0004	0.8271	0.0001
	Ad	DA-80 area 3 adularia line 1	38.423	0.007	15.574	0.003	18.822	0.003	2.0414	0.0001	0.8277	0.0001
	Py	DA-80 area 3 pyrite line 1	38.494	0.007	15.597	0.003	18.833	0.003	2.0440	0.0001	0.8284	0.0001
	Ad	DA-80 area 4 adularia line 1	38.470	0.007	15.591	0.003	18.834	0.003	2.0426	0.0001	0.8280	0.0001
	Alt	36-7-152.4 area 2 altaite spot 1	38.567	0.007	15.608	0.003	18.902	0.003	2.0404	0.0001	0.8260	0.0001
	Alt	36-7-152.4 area 2 altaite spot 2	38.518	0.007	15.592	0.003	18.890	0.003	2.0391	0.0001	0.8256	0.0001
	Gn	36-7-152.4 area 2 galena spot 1	38.573	0.007	15.610	0.003	18.909	0.003	2.0400	0.0001	0.8258	0.0001
	Sp	36-7-152.4 area 2 sphalerite line 1	nd		nd		nd		2.0399	0.0001	0.8251	0.0001
	Sp	36-7-152.4 area 2 sphalerite spot 1	38.559	0.007	15.609	0.003	18.903	0.003	2.0399	0.0001	0.8260	0.0001
	Gn	36-7-152.4 area 4 galena spot 1	38.526	0.007	15.599	0.003	18.881	0.003	2.0406	0.0001	0.8264	0.0001
	Alt	36-7-152.4 area 4 altaite spot 1	38.555	0.007	15.608	0.003	18.886	0.003	2.0415	0.0001	0.8266	0.0001
	Alt	36-7-152.4 area 3 altaite spot 1	38.568	0.007	15.608	0.003	18.903	0.003	2.0403	0.0001	0.8259	0.0001
	Gn	36-7-152.4 area 3 galena spot 1	38.562	0.007	15.607	0.003	18.901	0.003	2.0402	0.0001	0.8264	0.0001
Tuanjiegou	Gn	TJG-024 area 4 galena spot 1	38.221	0.007	15.544	0.003	18.317	0.003	2.0867	0.0001	0.8488	0.0001
	Gn	TJG-024 area 6 galena spot 1	38.203	0.007	15.539	0.003	18.311	0.003	2.0864	0.0001	0.8488	0.0001
	Gn	TJG-024 area 6 galena spot 2	38.190	0.007	15.539	0.003	18.307	0.003	2.0862	0.0001	0.8490	0.0001
	Py	TJG-002 area 1 pyrite line 1	38.170	0.003	15.525	0.003	18.272	0.003	2.0891	0.0004	0.8499	0.0001
	Py	TJG-002 area 1 fine-grained pyrite line 2	38.161	0.003	15.521	0.003	18.279	0.003	2.0878	0.0004	0.8494	0.0001
	Py	TJG-002 area 2 pyrite line 1	38.205	0.003	15.535	0.003	18.278	0.003	2.0903	0.0004	0.8501	0.0001
	Pl	TJG-002 area 3 plagioclase line 1	nd		nd		nd		2.1128	0.0004	0.8598	0.0001
	Pl	TJG-002 area 3 plagioclase line 2	nd		nd		nd		2.1177	0.0004	0.8626	0.0001
	Cal	TJG-006 area 1 calcite line 1	nd		nd		nd		2.1412	0.0004	0.8746	0.0001
	Cal	TJG-006 area 1 calcite line 2	nd		nd		nd		2.1376	0.0004	0.8705	0.0001
NIST SRM 981 (avg, n=12) solution introduction			36.711		15.489		16.935		2.1678		0.9148	
2s			0.008		0.002		0.003		0.0003		0.0001	
USGS PB-ISO-1G (avg, n=11) fs laser introduction			36.718		15.489		16.946		2.1667		0.9142	
2s			0.013		0.006		0.008		0.0004		0.0001	
USGS GSE-2G (avg, n=15) fs laser introduction			39.143		15.771		19.907		1.9656		0.7924	
2s			0.016		0.007		0.009		0.0003		0.0001	

Note: "nd" (not determined) was due to insufficient ^{204}Pb signal. SE = standard error.

This is the peer-reviewed, final accepted version for American Mineralogist, published by the Mineralogical Society of America.
The published version is subject to change. Cite as Authors (Year) Title. American Mineralogist, in press.
DOI: https://doi.org/10.2138/am-2022-8552. http://www.minsocam.org/

Table 4. Noble gas isotope results of fluid inclusions from Sandaowanzi, Yongxin, Dong'an, and Tuanjiegou in the North Heilongjiang Belt, NE China.

Deposit	Sample	Mineral	^{4}He (μcc/cc)	1σ	R/R_A	1σ	^{20}Ne (μcc/cc)	1σ	$^{20}Ne/^{22}Ne$	1σ	$^{21}Ne/^{22}Ne$	1σ	^{40}Ar (μcc/cc)	1σ	$^{40}Ar/^{36}Ar$	1σ	$^{38}Ar/^{36}Ar$	1σ
Sandaowanzi	170CM13	Quartz	0.151	0.009	0.219	0.023	0.042	1.18E-03	9.779	0.084	0.029	0.001	120.092	2.767	287.6	6.3	0.188	0.001
Sandaowanzi	130CM21-6	Quartz	0.010	0.001	0.340	0.036	0.003	7.03E-05	9.965	0.331	0.028	0.003	BDL	BDL	BDL	BDL	BDL	BDL
Sandaowanzi	130CM23-21	Quartz	0.417	0.024	0.064	0.007	BDL	BDL	BDL	BDL	BDL	BDL	BDL	BDL	BDL	BDL	BDL	BDL
Sandaowanzi	90CM4	Quartz	0.138	0.008	0.126	0.013	0.025	7.08E-04	9.926	0.360	0.029	0.001	37.555	0.865	289.9	6.4	0.188	0.001
Yongxin	180-29-232.5	Quartz	0.273	0.016	0.148	0.015	0.014	3.79E-04	10.120	0.582	0.029	0.001	50.210	1.157	278.8	6.1	0.188	0.001
Yongxin	175-20-141.1	Quartz	0.147	0.009	0.182	0.019	0.021	5.80E-04	9.818	0.659	0.029	0.001	58.703	1.353	303.0	6.7	0.189	0.001
Yongxin	175-25-186	Calcite	3.648	0.215	0.055	0.006	0.172	4.82E-03	9.846	0.135	0.029	0.001	478.419	11.023	268.3	5.9	0.192	0.001
Yongxin	175-13-133	Calcite	0.192	0.011	0.523	0.055	0.062	1.72E-03	10.123	0.236	0.029	0.001	198.494	4.573	278.8	6.1	0.194	0.001
Yongxin	175-24-188.3	Pyrite	0.472	0.028	1.698	0.155	0.038	1.06E-03	10.334	0.010	0.029	0.001	78.934	1.819	288.1	6.3	0.194	0.001
Dong'an	DA-103	Quartz	0.697	0.040	0.926	0.064	0.002	4.55E-05	10.048	0.107	0.027	0.003	BDL	BDL	BDL	BDL	BDL	BDL
Dong'an	DA-92	Quartz	0.093	0.005	0.028	0.003	0.002	6.58E-05	10.110	0.267	0.030	0.003	BDL	BDL	BDL	BDL	BDL	BDL
Dong'an	DA-115	Pyrite	2.261	0.131	0.036	0.004	0.006	1.50E-04	10.007	0.200	0.028	0.003	BDL	BDL	BDL	BDL	BDL	BDL
Dong'an	DA-61	Adularia	0.014	0.001	0.395	0.042	0.005	1.28E-04	10.023	0.342	0.028	0.003	BDL	BDL	BDL	BDL	BDL	BDL
Dong'an	DA-53	Adularia	0.009	0.001	0.478	0.050	0.004	1.05E-04	9.891	0.669	0.029	0.001	11.216	0.258	291.6	6.4	0.191	0.001
Dong'an	DA-23	Fluorite	0.525	0.030	0.752	0.077	0.003	8.81E-05	10.168	0.878	0.026	0.003	BDL	BDL	BDL	BDL	BDL	BDL
Dong'an	DA-125	Fluorite	0.356	0.021	0.248	0.025	0.011	3.13E-04	9.998	0.496	0.029	0.001	26.037	0.600	276.3	6.1	0.177	0.001
Tuanjiegou	TJG-019	Pyrite	0.006	0.000	0.448	0.047	0.003	9.40E-05	10.046	0.186	0.029	0.001	7.804	0.180	291.9	6.4	0.190	0.001
Tuanjiegou	TJG-015	Pyrite	0.010	0.001	0.135	0.014	0.002	4.80E-05	9.707	0.636	0.029	0.001	5.283	0.122	298.4	6.6	0.190	0.001
Tuanjiegou	TJG-006	Calcite	0.525	0.031	0.528	0.056	0.172	4.82E-03	9.956	0.002	0.029	0.001	906.175	20.879	248.8	5.5	0.178	0.001
Tuanjiegou	TJG-011	Quartz	0.328	0.019	0.097	0.010	0.024	6.64E-04	9.835	0.325	0.029	0.001	59.395	1.368	286.5	6.3	0.185	0.001

Note: BDL (below detection limit).

Always consult and cite the final, published document. See http:/www.minsocam.org or GeoscienceWorld

This is the peer-reviewed, final accepted version for American Mineralogist, published by the Mineralogical Society of America.
The published version is subject to change. Cite as Authors (Year) Title. American Mineralogist, in press.
DOI: https://doi.org/10.2138/am-2022-8552. http://www.minsocam.org/

16 Table 5. Homogenization temperatures and salinities of fluid inclusions from Sandaowanzi, Yongxin, Dong'an and Tuanjiegou in the
17 North Heilongjiang Belt, NE China.

Deposit	Stage	Host mineral	Type	Homogenization temperature (°C)	Salinity (NaCl eq. wt. %)	Reference
Sandaowanzi	Pre ore (I)	Quartz	L-V (N=150)	226–361	0.2–12.9	This study, Gao 2017, Gao et al., 2021
	Main ore (II-IV)	Quartz	L-V (N=213)	186–309	0.2–9.6	
	Post ore (V)	Quartz	L-V (N=50)	110–211	0.2–8.5	
	Secondary	Quartz	L-V (N=6)	167–216	0.2–0.7	Gao et al., 2021
Yongxin	Pre ore (I)	Quartz	L-V (N=8)	328–341	6.0–8.3	This study
	Main ore (II-IV)	Quartz	L-V (N=54)	178–297	3.0–9.2	
	Post ore (V)	Quartz	L-V (N=27)	117–207	2.2–11.2	
Dong'an	Pre ore (I)	Quartz	L-V (N=21)	260–290	0.2–4.9	This study, Gao et al., 2021
	Main ore (II-IV)	Quartz	L-V (N=53)	223–256	0.2–3.0	
	Post ore (V)	Fluorite	L-V (N=102)	120–190	0.4–3.2	This study, Zhi et al., 2016
	Secondary	Quartz	L-V (N=7)	164–210	0.5–1.1	Gao et al., 2021
Tuanjiegou	Pre ore (I)	Quartz	L-V (N=13)	261–280	1.8–2.2	This study
	Main ore (II-IV)	Quartz	L-V (N=34)	208–254	2.2–7.9	
	Post ore (V)	Calcite	L-V (N=10)	162–171	2.2–3.4	

Always consult and cite the final, published document. See http:/www.minsocam.org or GeoscienceWorld

This is the peer-reviewed, final accepted version for American Mineralogist, published by the Mineralogical Society of America.
The published version is subject to change. Cite as Authors (Year) Title. American Mineralogist, in press.
DOI: https://doi.org/10.2138/am-2022-8552. http://www.minsocam.org/

Table 6. Summary of lead and noble gas isotopes, fluid inclusion microthermometry, and the main features of Te-rich and Te-poor deposits in the North Heilongjiang Belt, NE China.

Type	**Te-rich**		**Te-poor**	
Block	Xing'an Block		Songliao Block	Jiamusi Massif
Location	Sandaowanzi	Yongxin	Dong'an	Tuanjiegou
Tonnage Au	22	20	24	80
Grade (g/t)	14	4	9	4
Au-bearing mineral	Quartz	Quartz, pyrite	Quartz	Quartz, pyrite
Age (Ma)	120	114	108	108
$^{206}Pb/^{204}Pb$	18.263-18.285	18.127-18.139	18.822-18.909	18.272-18.317
$^{207}Pb/^{206}Pb$	0.8486-0.8592	0.8557-0.8563	0.8251-0.8284	0.8488-0.8501
$^{208}Pb/^{206}Pb$	2.0824-2.1082	2.0935-2.0946	2.0384-2.0440	2.0866-2.0903
R/R_A (main stage)	0.080-1.030	0.810-1.800	0.395-0.478	0.135-0.448
R/R_A (early stage)	0.010-0.030	0.148-0.182	0.028-0.036	0.097
Temperature (main stage)	186-309	178-297	223-256	208-254
Salinity (main stage)	0.2-9.6	3.0-9.2	0.2-3.0	2.2-7.9
Magmatic Pb	Mafic	Mafic	Intermediate-felsic	Mafic
Rock Pb	K host rock, C-O basement	K host rock, C-O basement	K host rock, Tr-J and C-O basement	K host rock
t1 (Ga)	3.69-3.71	3.79-3.82	3.38-3.40	3.68-3.70
μ1	9.41-9.42	9.14-9.15	10.49-10.59	9.41-9.44
He_{mantle} (ore)%	1-15%	10-25%	1-5%	1-15%
Fluid evolution	Periodic magmatic inputs with Te-Au	Magmatic inputs with Te-Au	Meteoric water dominant	Periodic magmatic inputs with Au

Note: the $^{238}U/^{204}Pb$ ratio for the lead source (μ1) and the timings of crust formation for lead source (t1).

Always consult and cite the final, published document. See http:/www.minsocam.org or GeoscienceWorld

This is the peer-reviewed, final accepted version for American Mineralogist, published by the Mineralogical Society of America.
The published version is subject to change. Cite as Authors (Year) Title. American Mineralogist, in press.
DOI: https://doi.org/10.2138/am-2022-8552. http://www.minsocam.org/

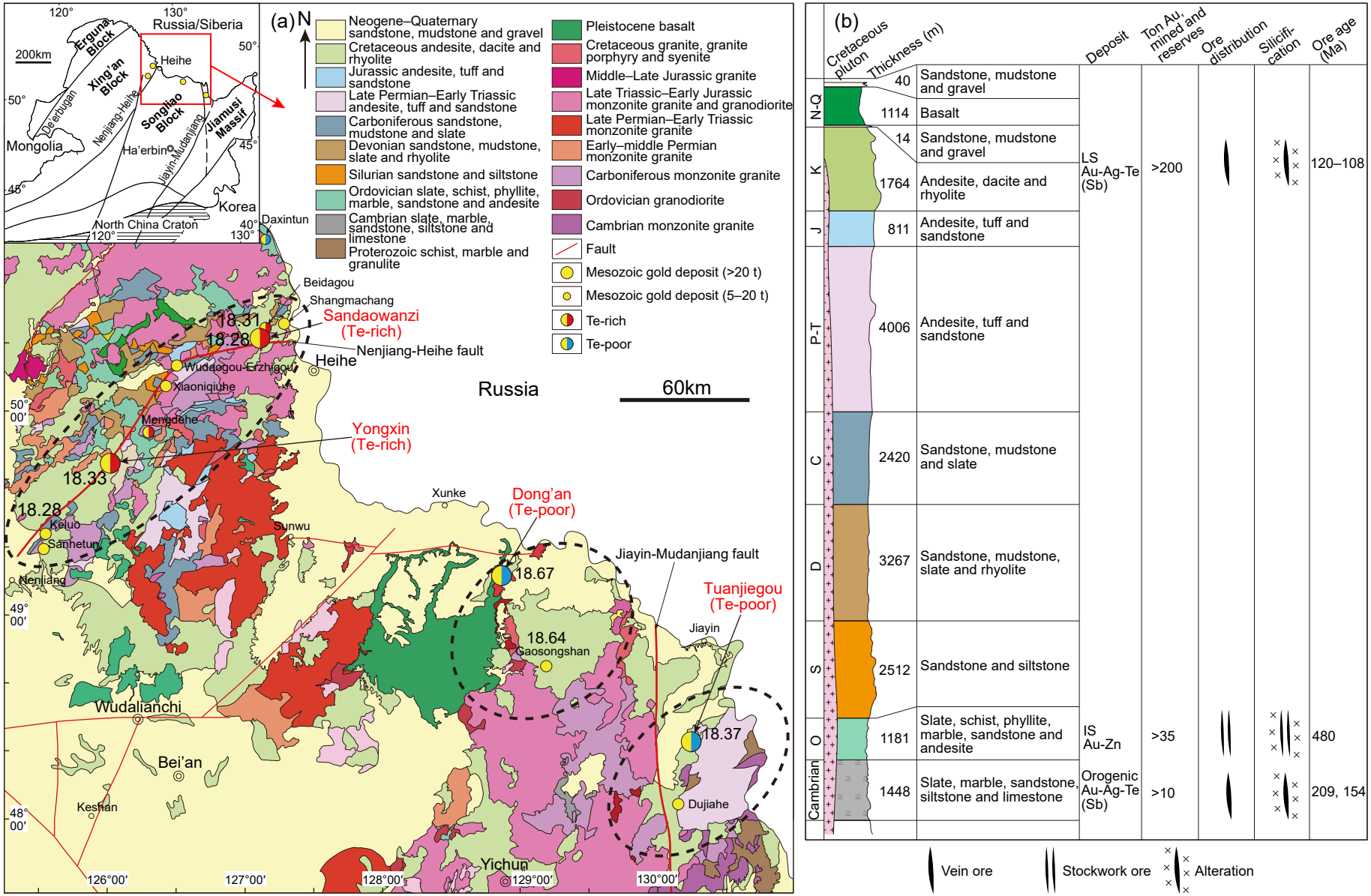

Figure 1

Always consult and cite the final, published document. See http:/www.minsocam.org or GeoscienceWorld

This is the peer-reviewed, final accepted version for American Mineralogist, published by the Mineralogical Society of America.
The published version is subject to change. Cite as Authors (Year) Title. American Mineralogist, in press.
DOI: https://doi.org/10.2138/am-2022-8552. http://www.minsocam.org/

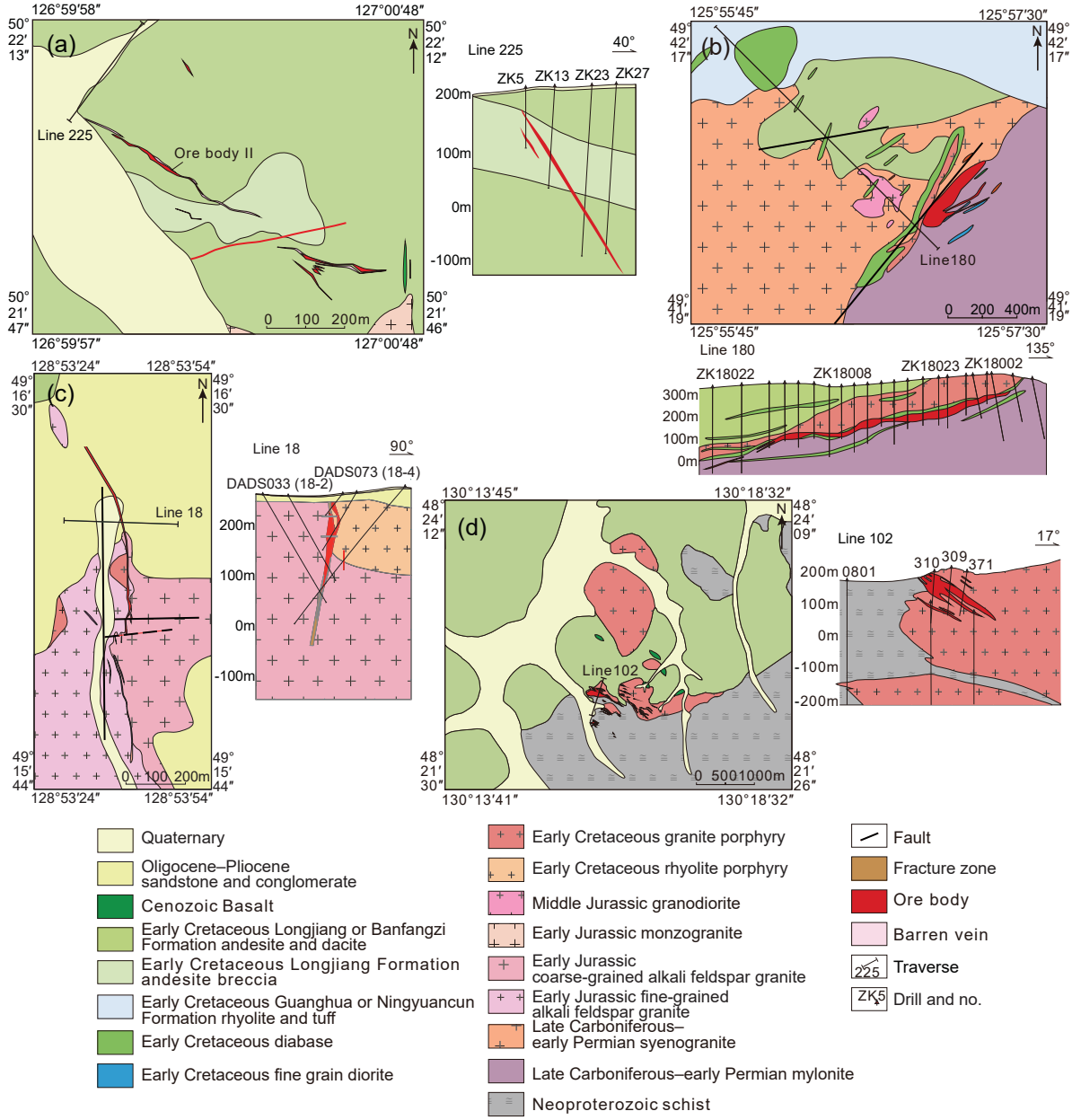

Figure 2

Always consult and cite the final, published document. See http:/www.minsocam.org or GeoscienceWorld

This is the peer-reviewed, final accepted version for American Mineralogist, published by the Mineralogical Society of America.
The published version is subject to change. Cite as Authors (Year) Title. American Mineralogist, in press.
DOI: https://doi.org/10.2138/am-2022-8552. http://www.minsocam.org/

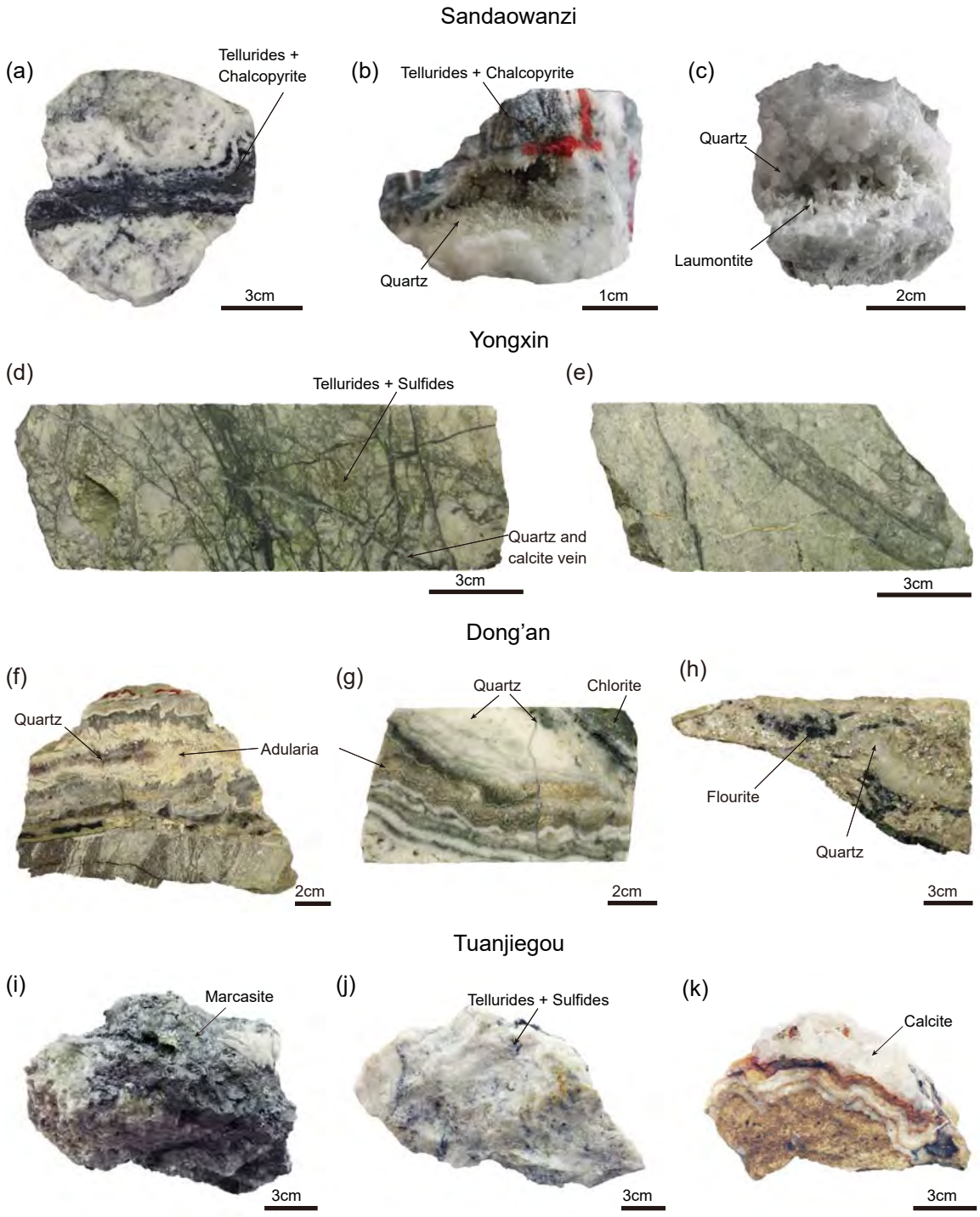

Figure 3

Always consult and cite the final, published document. See http:/www.minsocam.org or GeoscienceWorld

This is the peer-reviewed, final accepted version for American Mineralogist, published by the Mineralogical Society of America.
The published version is subject to change. Cite as Authors (Year) Title. American Mineralogist, in press.
DOI: https://doi.org/10.2138/am-2022-8552. http://www.minsocam.org/

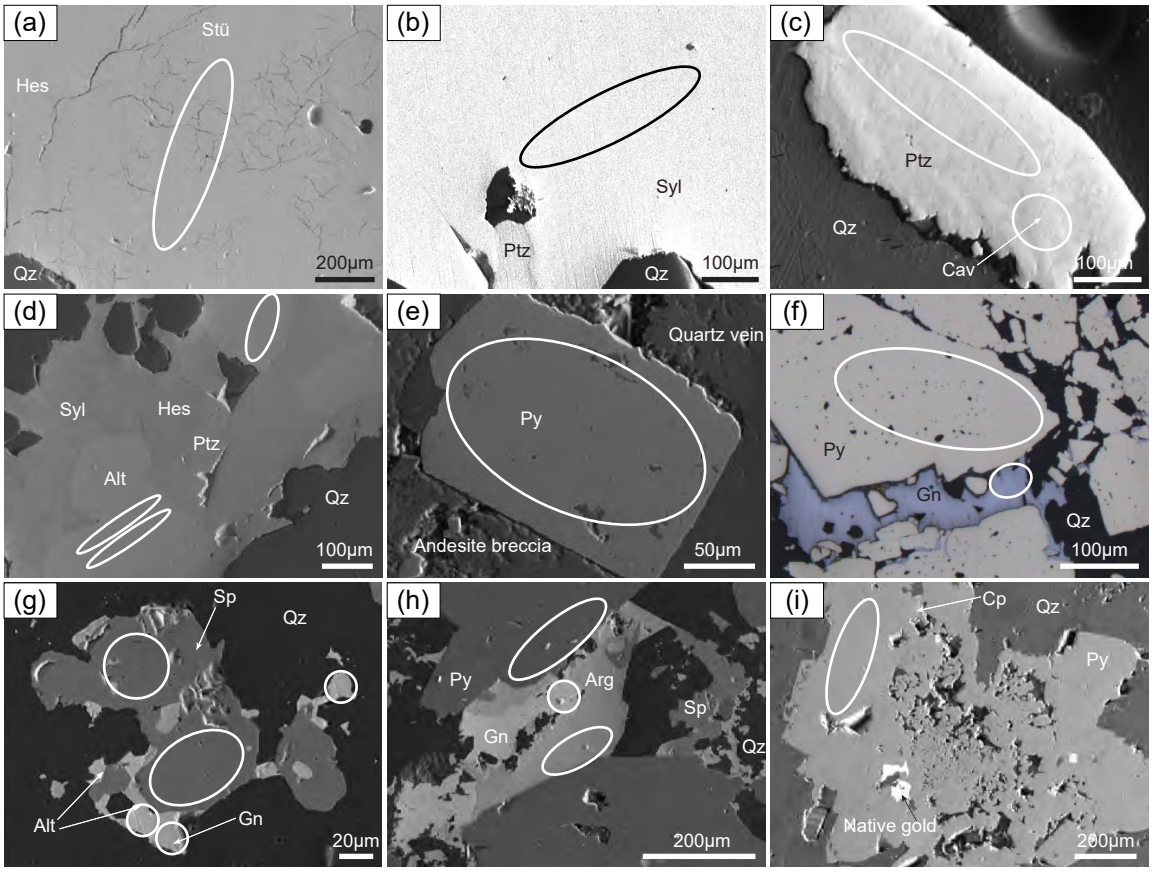

Figure 4

Always consult and cite the final, published document. See http:/www.minsocam.org or GeoscienceWorld

This is the peer-reviewed, final accepted version for American Mineralogist, published by the Mineralogical Society of America.
The published version is subject to change. Cite as Authors (Year) Title. American Mineralogist, in press.
DOI: https://doi.org/10.2138/am-2022-8552. http://www.minsocam.org/

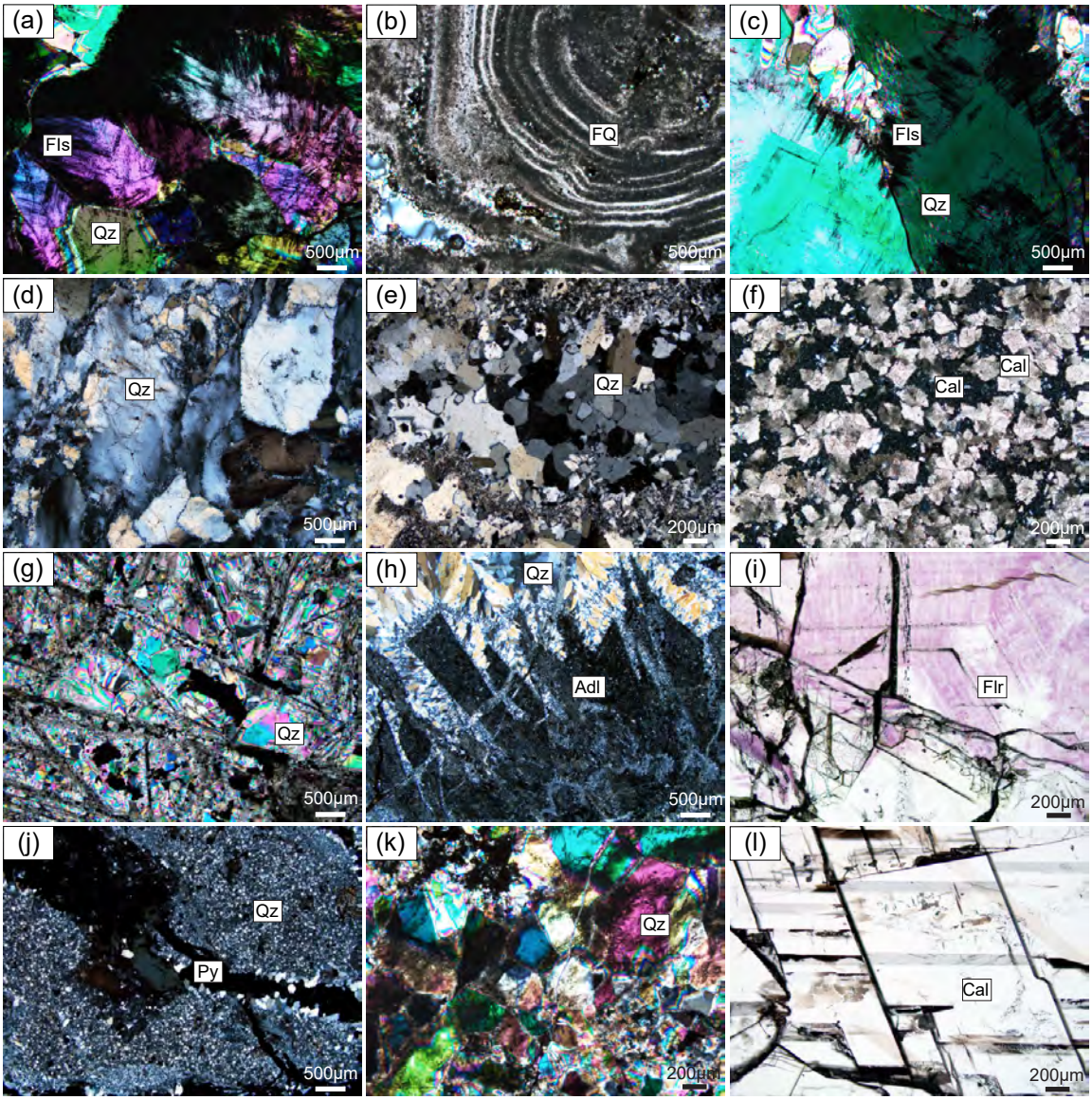

Figure 5

Always consult and cite the final, published document. See http:/www.minsocam.org or GeoscienceWorld

This is the peer-reviewed, final accepted version for American Mineralogist, published by the Mineralogical Society of America.
The published version is subject to change. Cite as Authors (Year) Title. American Mineralogist, in press.
DOI: https://doi.org/10.2138/am-2022-8552. http://www.minsocam.org/

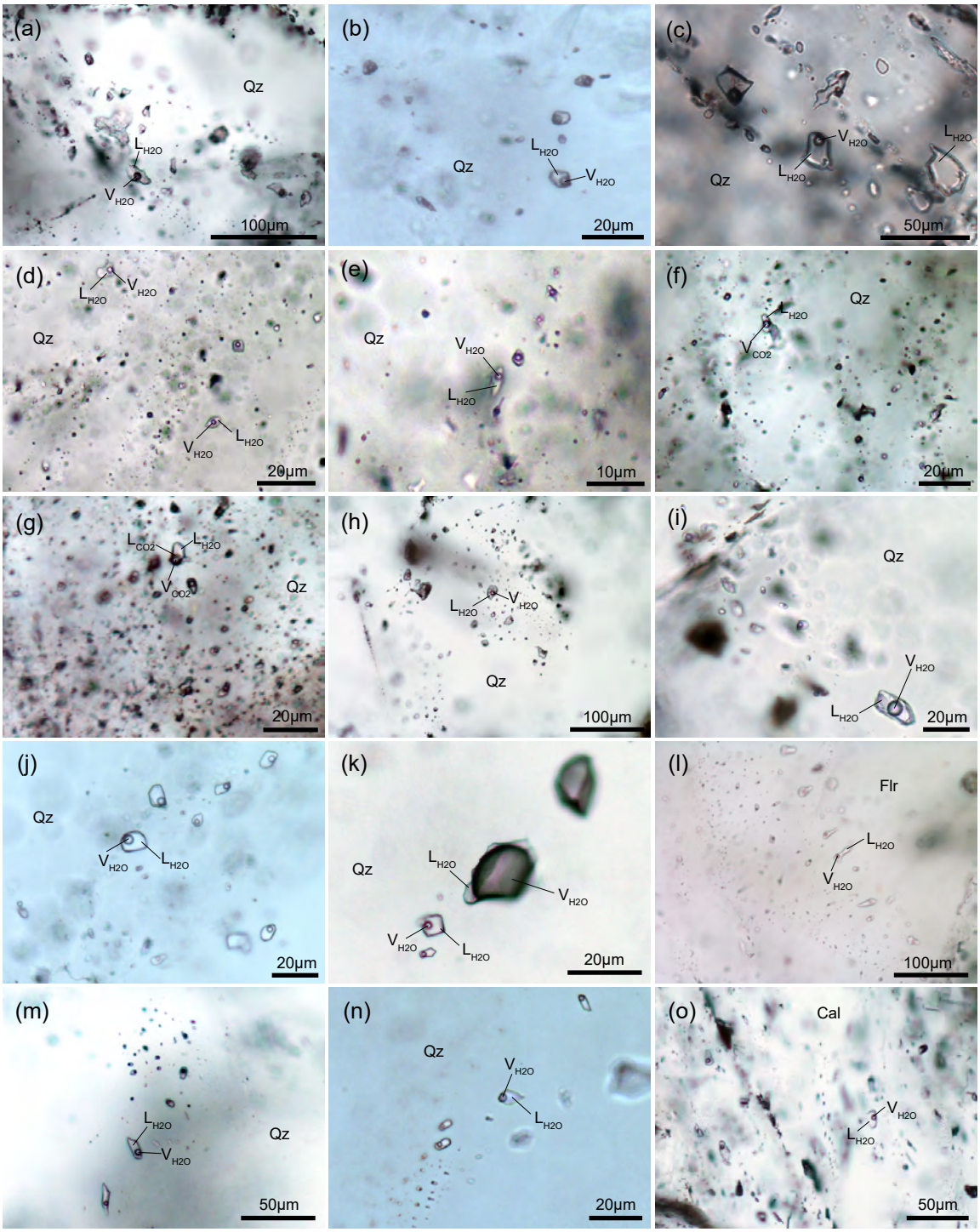

Figure 6

Always consult and cite the final, published document. See http:/www.minsocam.org or GeoscienceWorld

This is the peer-reviewed, final accepted version for American Mineralogist, published by the Mineralogical Society of America.
The published version is subject to change. Cite as Authors (Year) Title. American Mineralogist, in press.
DOI: https://doi.org/10.2138/am-2022-8552. http://www.minsocam.org/

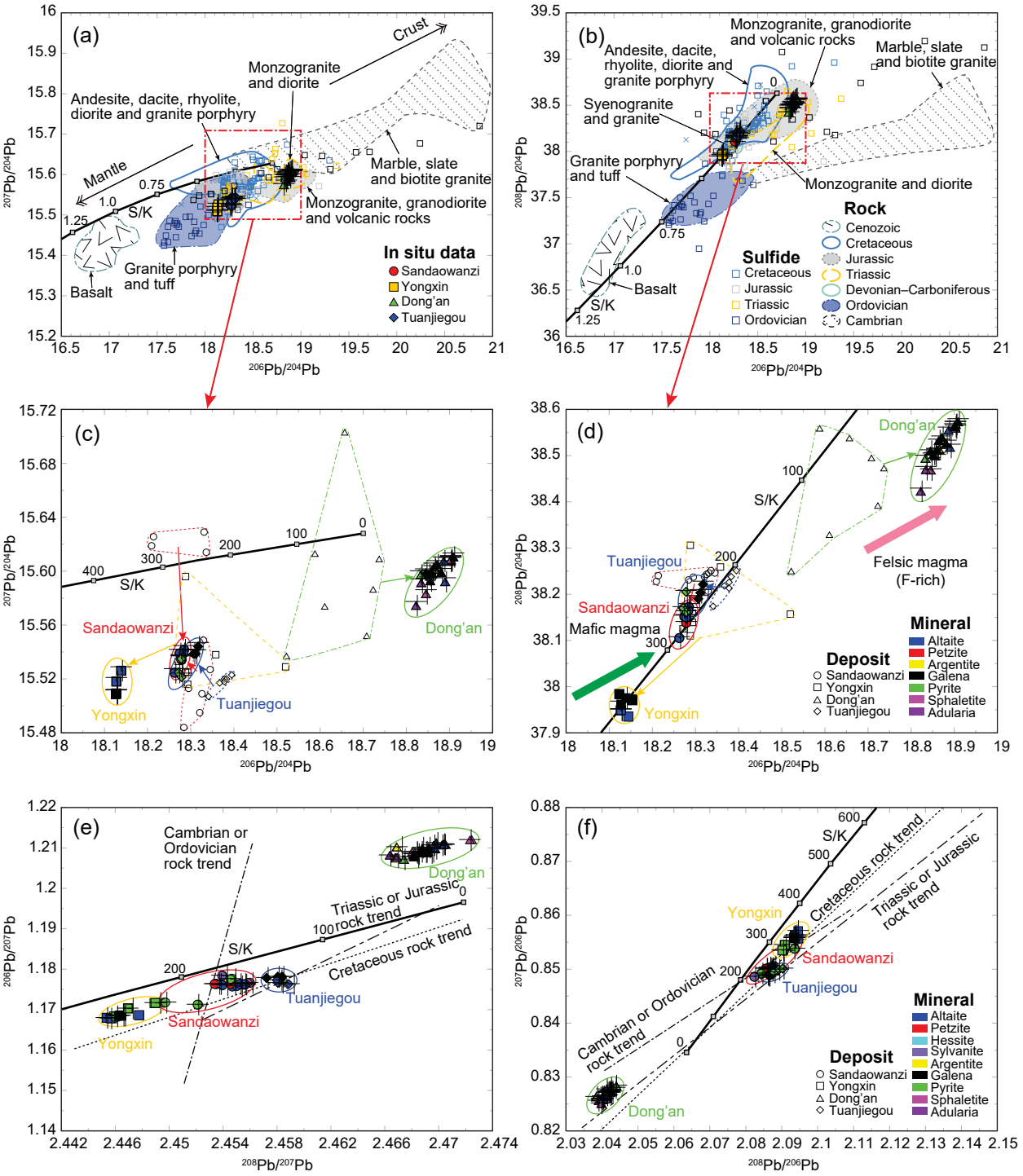

Figure 7

This is the peer-reviewed, final accepted version for American Mineralogist, published by the Mineralogical Society of America.
The published version is subject to change. Cite as Authors (Year) Title. American Mineralogist, in press.
DOI: https://doi.org/10.2138/am-2022-8552. http://www.minsocam.org/

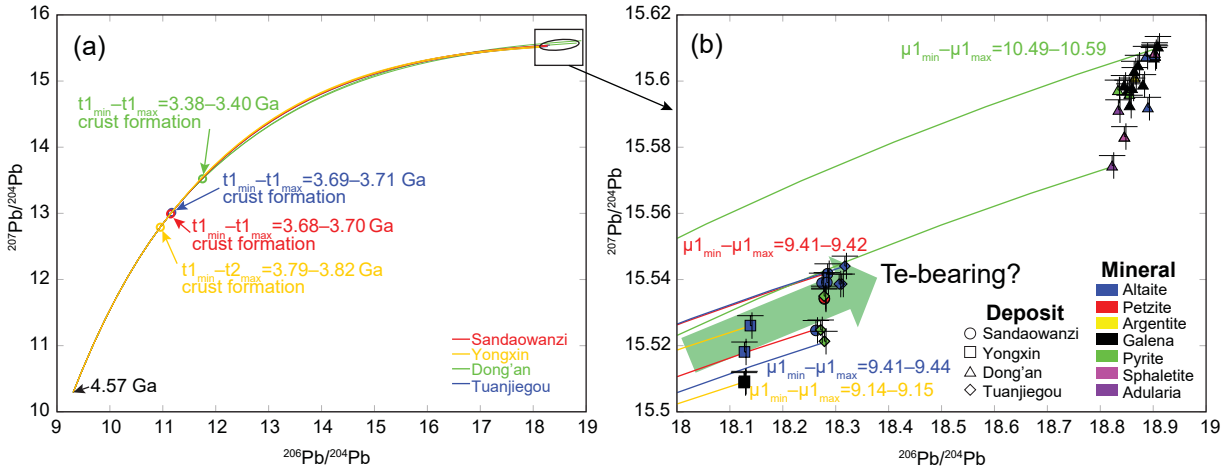

Figure 8

Always consult and cite the final, published document. See http:/www.minsocam.org or GeoscienceWorld

This is the peer-reviewed, final accepted version for American Mineralogist, published by the Mineralogical Society of America.
The published version is subject to change. Cite as Authors (Year) Title. American Mineralogist, in press.
DOI: https://doi.org/10.2138/am-2022-8552. http://www.minsocam.org/

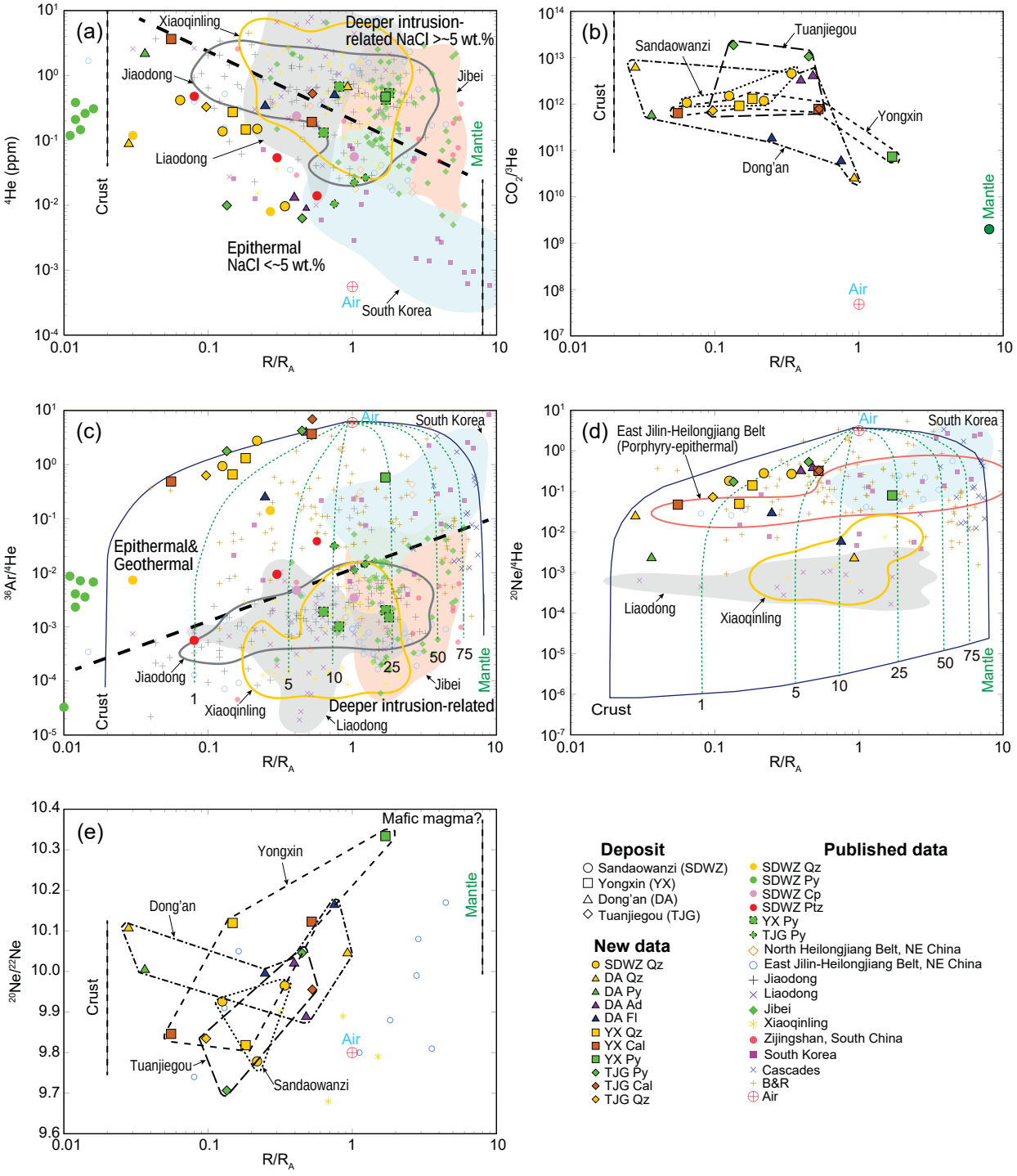

Figure 9

Always consult and cite the final, published document. See http:/www.minsocam.org or GeoscienceWorld

This is the peer-reviewed, final accepted version for American Mineralogist, published by the Mineralogical Society of America.
The published version is subject to change. Cite as Authors (Year) Title. American Mineralogist, in press.
DOI: https://doi.org/10.2138/am-2022-8552. http://www.minsocam.org/

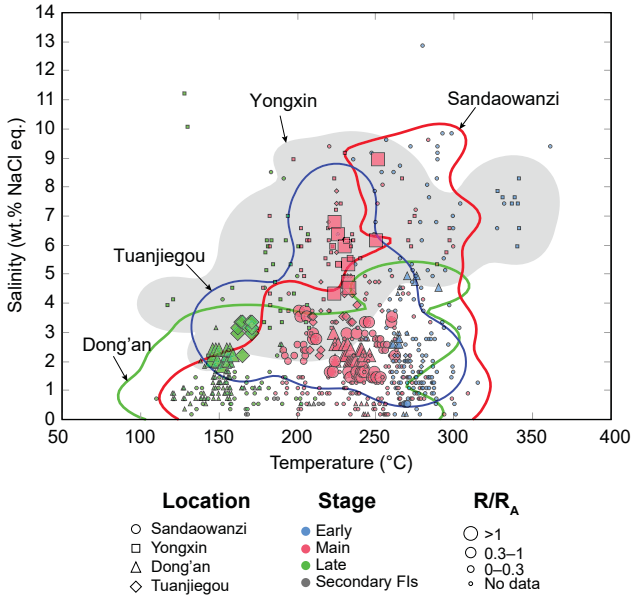

Figure 10

Always consult and cite the final, published document. See http:/www.minsocam.org or GeoscienceWorld

This is the peer-reviewed, final accepted version for American Mineralogist, published by the Mineralogical Society of America.
The published version is subject to change. Cite as Authors (Year) Title. American Mineralogist, in press.
DOI: https://doi.org/10.2138/am-2022-8552. http://www.minsocam.org/

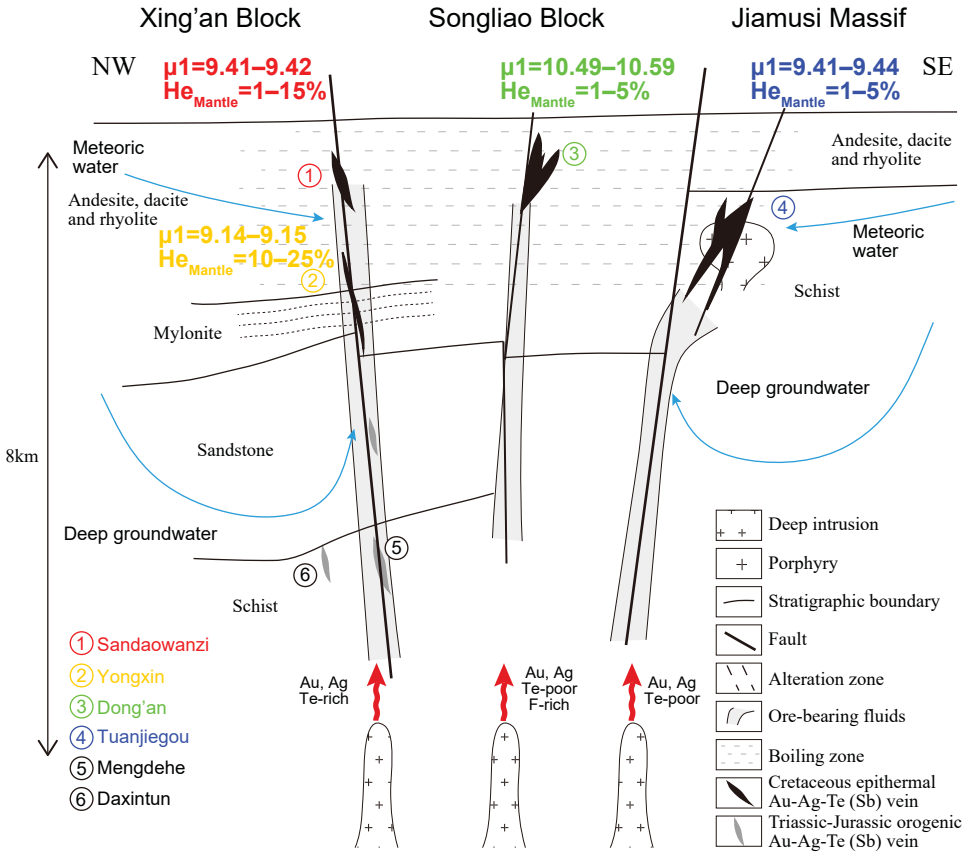

Figure 11

Always consult and cite the final, published document. See http:/www.minsocam.org or GeoscienceWorld